

Daytime variation of aerosol indirect effect for warm marine boundary layer clouds in the eastern north Atlantic

Shaoyue Qiu¹, Xue Zheng¹, David Painemal^{2,3}, Christopher R. Terai¹, and Xiaoli Zhou^{4,5}

¹Atmospheric, Earth and Energy Division, Lawrence Livermore National Laboratory, Livermore, California, USA

² Science Directorate, NASA Langley Research Center, Hampton, VA, USA

³ Analytical Mechanics Associates, Hampton, VA, USA

⁴Chemical Sciences Laboratory, NOAA, Boulder, CO, USA,

⁵Cooperative Institute for Research in Environmental Sciences (CIRES), University of Colorado, Boulder, CO, USA

Correspondence to: Shaoyue Qiu (qiu4@llnl.gov)

Submit to Atmospheric Chemistry and Physics July 21, 2023.

Abstract. Warm boundary layer clouds in the Eastern North Atlantic region exhibit significant diurnal variations in cloud properties. However, the diurnal cycle of the aerosol indirect effect (AIE) for these clouds remains poorly understood. This study takes advantage of recent advancements in the spatial resolution of geostationary satellites to explore the daytime variation of AIE by estimating the cloud susceptibilities to changes in cloud droplet number concentration (N_d). Cloud retrievals for four months of July (2018-2021) from SEVIRI on Meteosat-11 over this region are analyzed. Our results reveal a significant "U-shaped" daytime cycle in susceptibilities of cloud liquid water path (LWP), cloud albedo, and cloud fraction. Clouds are found to be more susceptible to N_d perturbations at noon and less susceptible in the morning and evening. The magnitude and sign of cloud susceptibilities depend heavily on the cloud state defined by cloud LWP and precipitation conditions. Non-precipitating thin clouds account for 44% of all warm boundary layer clouds in July and they contribute the most to the observed daytime variation. Non-precipitating thick clouds are the least frequent cloud state (10%), they exhibit more negative LWP and albedo susceptibilities compared to thin clouds. Precipitating clouds are the dominant cloud state (46%), but their cloud susceptibilities show minimal variation throughout the day.

We find evidence that the daytime variation of LWP and albedo susceptibilities for non-precipitating clouds are influenced by a combination of the diurnal transition between non-precipitating thick and thin clouds and the "lagged" cloud responses to N_d perturbations. The daytime variation in cloud fraction susceptibility for non-precipitating thick clouds can be attributed to the daytime variation in cloud morphology (e.g., overcast or broken). The dissipation and development of clouds do not adequately explain the observed variation in cloud susceptibilities. Additionally, daytime variation of cloud susceptibility is primarily driven by variation in the intensity of cloud response rather than the frequency of occurrence of cloud states. Our results imply that polar-

38 orbiting satellites with overpass time at 13:30 local time underestimate daytime mean value of cloud susceptibility,
39 as they observe susceptibility daily minima in the study region.

40

41

42 1. Introduction

43 Warm boundary layer clouds, including stratus, stratocumulus, and cumulus clouds, are prevalent over the
44 sub-tropical oceans, account for over 30% of the global annual mean cloud coverage (Warren et al., 1988; Wood,
45 2012). These clouds have a significant net negative radiative forcing on the surface radiation budget. However, our
46 understanding of the aerosol indirect effect (AIE) on these clouds, particularly the impact of aerosols on cloud
47 amount, brightness, and lifetime, remains a significant source of uncertainty in estimating the radiative forcing from
48 human activities. The AIE plays a critical role in the Earth's radiation budget through its interactions with clouds. It
49 consists of two effects: the Twomey effect, which involves the increase in cloud droplet number from increasing
50 aerosols, and leads to an increase in cloud albedo (α_c) from smaller droplets when the cloud liquid water path
51 (LWP) is held constant (Twomey, 1977), and the cloud adjustment effect, which encompasses the impact of aerosols
52 on cloud amount, cloud water, and α_c through modulating cloud processes (e.g., Albrecht, 1989; Xue and Feingold,
53 2006; Chen et al., 2014; Gryspeerdt et al., 2019). The cloud adjustment effect is highly variable with large
54 uncertainties in signs and magnitudes depending on cloud state, boundary layer, and meteorological conditions
55 among other factors (e.g., Han et al., 2002; Wang et al., 2003; Small et al., 2009; Sato et al., 2018).

56 Previous studies have made significant progress in identifying different cloud processes and feedback
57 mechanisms to explain the responses of CF, LWP, and α_c to aerosol perturbations (e.g., as summarized in Steven
58 and Feingold, 2009; Fan et al., 2016; Gryspeerdt et al., 2019). The cloud adjustment effect is influenced by two key
59 feedback mechanisms: precipitation suppression, and sedimentation-evaporation-entrainment.

60 Under clean conditions and for clouds predominantly precipitating, an increase in the cloud droplet number
61 concentration (N_d) and associated decrease in droplet sizes, reduces precipitation efficiency, and decreases water
62 loss from precipitation. Consequently, this promotes an increase in cloudiness and cloud LWP (Albrecht, 1989; Qian
63 et al., 2009; Li et al., 2011; Terai et al., 2012, 2015). For non-precipitating clouds, decreased cloud drop size due to
64 increases in N_d impacts CF and LWP through their impact on the entrainment rate. A decrease in cloud droplet size
65 diminishes the sedimentation rate in clouds, causing an accumulation of cloud water near the cloud top. This
66 increased cloud water in the entrainment zone enhances cloud-top radiative cooling, entrainment rate, and
67 evaporation, resulting in a decrease in CF and cloud LWP (Bretherton et al., 2007; Chen et al., 2014; Toll et al.,
68 2019; Gryspeerdt et al., 2019).

69 Additionally, the faster evaporation rates from smaller droplets enhance cloud-top cooling, downward
70 motion in clouds, total kinetic energy, and horizontal buoyancy gradient. The processes listed above, in turn,
71 increase evaporation and entrainment rate and, thus, forming a positive feedback loop (Wang et al., 2003; Xue and
72 Feingold, 2006; Small et al., 2009; Toll et al., 2019). Furthermore, among non-precipitating clouds, thick clouds
73 with larger LWP exhibit stronger cloud-top longwave radiative cooling rate and therefore stronger cloud-top
74 entrainment rate (e.g., Sandu et al., 2008, Williams and Igel, 2021). Therefore, the classification of cloud states (e.g.,
75 precipitating conditions and thickness) is essential for accurately quantifying the AIE and discerning opposing cloud
76 processes. In this study, we classify cloud states based on the LWP- N_d parameter space, as these variables provide
77 the most informative metrics for cloud susceptibility (Zhang et al., 2022).

78 This study focuses on the Eastern North Atlantic (ENA) region, where the U.S. Department of Energy
79 (DOE) Atmospheric Radiation Measurement program (ARM) deployed the ground-based user facility at the Azores
80 archipelago (Mather and Voyles, 2013). During the summer over ENA region, warm boundary layer clouds exhibit
81 pronounced diurnal variations in their properties and cloud states. For example, based on ARM surface radar and
82 lidar observations, the frequency of stratocumulus clouds is highest at night, accompanied by an increase in the
83 fraction of precipitating clouds. Throughout the daytime, both cloud fraction and precipitation fraction experience a
84 slight decrease, followed by an increase after sunset (Remillard et al, 2012). The retrieved cloud microphysical
85 properties from ARM ground-based observations show similar “U-shaped” diurnal variations in cloud LWP, liquid
86 water content, and optical thickness (Dong et al., 2014). Additionally, numerical studies have revealed a distinct
87 diurnal cycle of AIE for marine stratocumulus clouds, attributed to changes in cloud properties and boundary layer
88 thermodynamic conditions (e.g., Sandu et al., 2008, 2009). However, observational analyses based on the ground-
89 based observations at the ENA site or in-situ measurements from field campaigns are often based on a few cases
90 with limited samples and insufficient spatial coverage (e.g., Liu et al., 2016; Wang et al., 2021; Zheng et al., 2022).
91 There have been few observational studies investigating the diurnal cycle of AIE in the ENA region. With recent
92 advancements in the spatial resolution of geostationary satellites, this study aims to investigate the diurnal variation
93 of the AIE in warm boundary layer clouds over the ENA region and gain a better understanding of the underlying
94 mechanisms.

95 Both cloud properties and meteorological conditions have substantial spatiotemporal variability and distinct
96 diurnal variations. Furthermore, changes in meteorological conditions can in turn influence cloud and aerosol
97 properties. One of the main challenges in understanding the AIE lies in isolating the impacts of the confounding
98 meteorological drivers on clouds and aerosols from AIE on clouds. To address this challenge, Gryspeerdt et al.
99 (2016) proposed the use of N_d as an intermediary variable for AIE, instead of using aerosol optical depth (AOD) or
100 aerosol index. The use of N_d circumvents the well-known dependency of AOD on CF and surface wind speed,
101 which does not necessarily reflect actual changes in aerosol loading. Moreover, the control of relative humidity and
102 aerosol type on AOD prevents to establish a direct link between AOD and aerosol concentration or cloud
103 condensation nuclei (CCN).

104 Another common method to disentangle meteorological impacts is to sort the controlling meteorological
105 factors of cloud state, such as relative humidity, lower tropospheric stability, vertical velocity, and examine the AIE
106 accordingly (e.g., Chen et al., 2014; Gryspeerdt et al., 2019). However, this approach overlooks important
107 information, including the frequency of occurrence of specific environmental conditions, the spatiotemporal co-
108 variation of meteorological factors, and the correlations among them. Zhou et al. (2021) and Zhang et al. (2022)
109 proposed a new method to estimate the cloud susceptibility within a confined space (e.g., a $1^\circ \times 1^\circ$ or $2^\circ \times 2^\circ$ grid
110 box) of each satellite snapshot by assuming consistent meteorological conditions within this spatial domain.
111 Additionally, it is important to note that meteorological conditions influence albedo susceptibility by altering the
112 frequency of occurrence of different cloud states (e.g., precipitating and non-precipitating). Specifically, within a
113 particular cloud state, meteorological conditions offer limited information regarding cloud susceptibility (Zhang et
114 al, 2022).

115 The second main source of uncertainty in observational AIE studies arise from inferring processes in a
116 temporally evolving system based on snapshots of observations (Mülmenstädt and Feingold, 2018). Due to the
117 limited temporal or spatial resolution of the observations, most studies assume a Markovian system, where clouds
118 and AIE are assumed to only relate to the current state of the system and have no memory of the past states.
119 However, this assumption contradicts the nature of the cloud system. Observational and modeling studies have
120 shown that aerosol-cloud interaction processes take hours to reach the equilibrium state and the sensitivity of AIE is
121 time dependent. For instance, Glassmeier et al. (2021) applied a Gaussian-process emulation and derived the
122 adjustment equilibration timescale for LWP to be ~ 20 hours. By tracking the ship tracks in satellite observations,
123 Gryspeerd et al. (2021) found a similar AIE timescale of ~ 20 hours or longer and the magnitude of LWP
124 susceptibility increases with time. In addition, Christensen et al. (2020) discovered that influence of aerosols on
125 cloud LWP, CF, and cloud top height persists two to three days by tracking cloud systems in satellite observations.
126 In summary, the sensitivity of cloud responses to N_d perturbations changes with time and, thus, the assumption that
127 AIE has no memory of its past state is inadequate. Nonetheless, the direct evaluation of the impact of cloud memory
128 on the quantified cloud susceptibility remains unexplored, to the best of our knowledge.

129 To facilitate a process-level understanding of the drivers behind the diurnal variation of AIE for warm
130 boundary layer clouds, we will classify these clouds into three states: precipitating clouds, non-precipitating thick
131 clouds, and non-precipitating thin clouds. We investigate the changes in both the frequency of occurrence of cloud
132 states and the magnitude of AIE for different cloud states throughout the day. Additionally, we document the
133 temporal changes in cloud state within each fixed $1^\circ \times 1^\circ$ grid box and quantify the influences of cloud memory and
134 state transition on AIE. Section 2 describes the datasets as well as the methodology employed to quantify cloud
135 susceptibilities, distinguish precipitating clouds from the satellite retrievals, and track cloud states. We present our
136 results in Section 3. Section 3.1 characterizes the general conditions of warm boundary clouds over the ENA region
137 during the summer. Section 3.2 introduces the LWP- N_d parameter space and illustrates the dependence of cloud
138 responses to N_d perturbations on cloud states. We then discuss the mean daytime variation of cloud susceptibilities
139 for all cloud states in Section 3.3, followed by an analysis of the AIE daytime variation for each cloud state and the
140 impact of the state transition on AIE in Section 3.4. In Section 3.5, we decompose the contributions to the daytime
141 variation of cloud susceptibility into two components, one is from changes in the frequency of occurrence of
142 different cloud states and the other is from changes in the intensity of AIE during the day. Section 4 includes
143 discussions on the similarities and differences in findings between this study and previous studies of AIE and
144 Section 5 is the summary and conclusions of this study.

145 **2. Dataset and Methodology**

146 We use cloud retrievals derived from the Spinning Enhanced Visible InfraRed Imager (SEVIRI) on
147 Meteosat-11, with a spatial resolution of 3 km at nadir and a half-hourly temporal resolution over the ENA region
148 ($33\text{-}43^\circ\text{N}$, $23\text{-}33^\circ\text{W}$). SEVIRI cloud products are derived using the Satellite CLOUD and Radiation Property retrieval
149 System (SatCORPS) algorithms (e.g., Painemal et al., 2021), based on the methods applied by the Clouds and the

150 Earth’s Radiant Energy System (CERES) project, and specifically tailored to support the ARM program over the
 151 ARM ground-based observation sites (Minnis et al. 2011, 2020). Given the purpose of this study on quantifying the
 152 AIE on warm boundary layer clouds, we focus on four months of July (2018-2021), a period that coincides with the
 153 highest frequency of occurrence of warm boundary layer clouds over the ARM ENA site (Rémillard et al. 2012;
 154 Dong et al., 2014, 2023).

155 The cloud mask algorithm implemented in SatCORPS is described in Trepte et al. (2019). SatCORPS cloud
 156 properties are based on the shortwave-infrared split-window technique during daytime (VISST, Minnis et al. 2011,
 157 2020), with cloud optical depth (τ) and effective radius (r_e) being derived using an iterative process that combines
 158 reflectance and brightness temperatures from the 0.64 μm and 3.9 μm channels. Cloud LWP is computed from τ and
 159 r_e using the formula $LWP = \frac{4r_e\tau}{3Q_{ext}}$, where Q_{ext} represents the extinction efficiency and assumed constant of 2.0
 160 (Minnis et al. 2011, 2020). The top-of- atmosphere (TOA) broadband shortwave α_c is derived from an empirical
 161 radiance-to-broadband conversion using the satellite imager’s visible channel and CERES Single Scanning Footprint
 162 (SSF) shortwave fluxes, and dependent on solar zenith angle and surface type (Minnis et al. 2016). Cloud top height
 163 computation follows the methodology in Sun-Mack et al. (2014).

164 To validate the Meteosat-11 retrieved cloud mask and the detection of boundary layer clouds, we compare
 165 the boundary layer cloud fractions derived from Meteosat-11 with the ground-based observations at the ARM ENA
 166 site. As seen in Fig.S1, both the diurnal variation and the mean CF of Meteosat-11 agree well with ARM
 167 observations. More details on the methodology for the evaluation study are included in the supplementary material.

168 Our analysis focuses on warm boundary layer clouds with cloud tops below 3km and a liquid cloud phase.
 169 To focus specifically on boundary layer cloud cases without including the edges of deep clouds, we apply a stricter
 170 threshold than merely using the pixel-level cloud top height. We define boundary layer clouds as those with 90% of
 171 their cloud tops below 3km, labeling all contiguous cloudy pixels as distinct cloud objects.

172 Cloud N_d is retrieved based on the adiabatic assumptions for warm boundary layer clouds, as in Grosvenor
 173 et al. (2018) according to the following equation:

$$174 \quad N_d = \frac{\sqrt{5}}{2\pi k} \left(\frac{f_{ad}c_w\tau}{Q_{ext}\rho_w r_e^5} \right)^{1/2} \quad (1)$$

175 In Equation (1), k represents the ratio between the volume mean radius and r_e , assumed to be constant of 0.8 for
 176 stratocumulus; f_{ad} is the adiabatic fraction of the observed liquid water path and assumed to be 0.8 for
 177 stratocumulus clouds (Brenquier et al., 2011; Zuidema et al., 2012); c_w is the condensation rate, which is a function
 178 of temperature and pressure; Q_{ext} is the extinction coefficient, approximated as 2 in this study; and ρ_w is the density
 179 of liquid water. While the different components of Eq. (1) could contribute to the uncertainties in N_d , errors in r_e are
 180 the dominant drivers in Eq. (1) (Grosvenor et al., 2018).

181 To minimize uncertainties associated with bias in satellite cloud microphysical retrievals, we only select
 182 pixels with a minimum r_e of $3\mu\text{m}$, a minimum τ of 3, and a solar zenith angle (SZA) of less than 65° (e.g., Painemal
 183 et al., 2013; Painemal, 2018; Zhang et al., 2022). The SZA threshold of 65° was chosen to minimize biases observed
 184 at high solar zenith angle in r_e and τ (e.g., Grosvenor & Wood, 2014; Grosvenor et al., 2018).

185 In addition, to reduce uncertainties associated with the adiabatic assumption in the N_d retrieval, we
186 implement a filtering process. For each cloud, we exclude cloudy pixels at the cloud edge, defined as those adjacent
187 to cloud-free pixels, following a similar sampling strategy suggested by Gryspeerdt et al. (2022). Therefore, all
188 cloud properties in this study refer to the properties of cloud body without cloud edge. It is worthy of note that
189 shallow cumulus clouds with diameters smaller than 9km are not included. The removal of cloud-edge pixels
190 accounts for ~14% of the cloudy pixels. Furthermore, we removed grid boxes containing islands due to the
191 uncertainties in Meteosat retrievals over contrasting underlying surface. Lastly, to avoid unrealistically large
192 retrievals, we eliminate pixels with the retrieved N_d values exceeding 1000 cm^{-3} , which constituted only 0.002% of
193 the data.

194 Cloud susceptibility is quantified as the slope between cloud properties and N_d using a least-square
195 regression. As found by Arola et al. (2022) and Zhou and Feingold (2023), the retrieved cloud susceptibilities are
196 sensitive to small-scale cloud heterogeneity, the co-variability between cloud properties and N_d , and the spatial scale
197 of cloud organization. To reduce biases resulting from heterogeneity and co-variability, we first average the 3-km
198 pixel-level cloud retrievals and N_d (Eq. 1) to a regular $0.25^\circ \times 0.25^\circ$ grid for each half-hourly time step.

199 To further mitigate the impact from co-variability between cloud properties and N_d at larger spatiotemporal
200 scales, cloud susceptibility is estimated within a $1^\circ \times 1^\circ$ grid box at each satellite time step (e.g., Zhang et al, 2022).
201 Moreover, estimating the cloud susceptibility over a confined space also help to constrain the meteorological
202 impacts on AIE, with the assumption of a homogeneous meteorological condition within this spatial scale. Next,
203 susceptibilities are calculated using the 0.25° smoothed data if the number of data points within the $1^\circ \times 1^\circ$ box
204 exceeds six (from a maximum of 16 data points). It is important to note that when computing the $0.25^\circ \times 0.25^\circ$
205 averaged cloud properties, only data from cloudy pixels are used to ensure that the estimated susceptibility is not
206 weighted by CF or impacted by satellite artifacts. Lastly, due to the minimal spatial variability of cloud
207 susceptibility in the study region, the 1° cloud susceptibility is averaged over the study region ($33\text{-}43^\circ\text{N}$, $23\text{-}33^\circ\text{W}$)
208 to characterize the daytime variation of AIE. Additionally, results and conclusions of this study are not sensitive to
209 the size of the box calculating the cloud susceptibility (e.g., over a $0.8^\circ \times 0.8^\circ$ box or over a $1.5^\circ \times 1.5^\circ$ box, not
210 shown).

211 Because of the nonlinear relationships between LWP and N_d , the LWP susceptibility is defined as the slope
212 in logarithmic scale, that is: $d\ln(LWP)/d\ln(N_d)$ (e.g., Gryspeerdt et al. 2019). The albedo susceptibility is
213 estimated as the slope between α_c and $\ln(N_d)$, equivalent to $d\alpha_c/d\ln(N_d)$ (e.g., Painemal 2018). Lastly, the CF
214 susceptibility is estimated as $dCF/d\ln(N_d)$. The mean CF is defined as the fraction of cloudy pixels excluding
215 cloud edge to the sum of cloudy and clear pixels within each $0.25^\circ \times 0.25^\circ$ box. Due to the highly variable nature of
216 CF, the variability in the 0.25° CF could arise from quantifying edges or centers of the same cloud layer rather than
217 N_d perturbations. To assess the potential influence of cloud morphology on the retrieved CF susceptibility, we
218 excluded any $1^\circ \times 1^\circ$ scene meeting the following three criteria: 1) the difference between the maximum and
219 minimum 0.25° CF greater than 0.9, 2) the variation in the $0.25^\circ N_d$ less than 60 cm^{-3} , and 3) the 0.25° CF in the
220 $1^\circ \times 1^\circ$ box sample the same cloud. The 0.9 and 60 cm^{-3} thresholds represent ~45% of the data. With the three
221 thresholds combined, a total of 17,000 scenes were removed, which accounts for ~24% of the total samples.

222 Removing these scenes does not change the conclusions of CF susceptibility in this study (not shown), which
 223 demonstrates that cloud morphology, has minimal impact on the retrieved CF susceptibility. Furthermore, as we
 224 removed N_d retrievals at cloud edge where N_d likely suffers large uncertainties, cloudy pixels at cloud edge are set
 225 as clear for consistency in the calculation of the CF susceptibility. Removing the cloud edge decreases the four-
 226 month mean CF for warm boundary layer clouds from 21.6% to 19.0%.

227 The susceptibility of the shortwave radiative fluxes to N_d (F_0) is estimated as the sensitivity of the TOA
 228 shortwave upward radiative flux (SW_{TOA}^{up}) to N_d perturbations (e.g., Chen et al. 2014; Painemal 2018; Zhang et al.
 229 2022). The mean SW_{TOA}^{up} over a $1^\circ \times 1^\circ$ grid box is estimated using Eq. (2), with the assumption that the clear-sky
 230 albedo over the ocean is small compared to the cloud albedo:

$$231 \quad \overline{SW_{TOA}^{up}} = \overline{SW_{TOA}^{dn}} \cdot \overline{\alpha_c} \cdot \overline{CF}, \quad (2)$$

232 where SW_{TOA}^{dn} is the grid-box mean TOA shortwave downward radiative flux, which is estimated based on the
 233 latitude, longitude, date, and overpass time of each pixel, α_c and CF are the grid-box mean values. Then, F_0 is
 234 estimated using the calculated α_c and CF susceptibilities, and the $1^\circ \times 1^\circ$ grid-box mean cloud properties as shown
 235 in the equation below:

$$236 \quad F_0 = -\frac{dSW_{TOA}^{up}}{d\ln(N_d)} = -\overline{SW_{TOA}^{dn}} \cdot \left(-\frac{d\alpha_c}{d\ln(N_d)} \cdot \overline{CF} + \frac{dCF}{d\ln(N_d)} \cdot \overline{\alpha_c} \right). \quad (3)$$

237 F_0 is in the unit of $W m^{-2} \ln(N_d)^{-1}$, and a positive value indicates a decrease in the SW_{TOA}^{up} , which is a *warming*
 238 effect at the surface.

239 To minimize uncertainties in the linear regression for the estimated susceptibility, we analyze regressions
 240 that exhibited a goodness of fit exceeding the 95% confidence interval (i.e., $\chi^2 < \chi_{0.95,c}^2$), and an absolute
 241 correlation coefficient greater than 0.2 (e.g., Painemal, 2018; Zhang et al., 2022). There is a total of $\sim 115,000$
 242 samples of the 1° cloud susceptibilities in this study, applying the goodness of fit thresholds result in exclusions of \sim
 243 33,000- 43,000 samples for different susceptibilities, which are ~ 28 -37% of the data. Sensitivity test shows that
 244 including cases that fail the goodness of fit test will not change the results and conclusions of this study (not shown).
 245 Specifically, including these cases decrease the magnitude of cloud susceptibilities for all three cloud states, but the
 246 signs of cloud responses to N_d perturbations remain consistent.

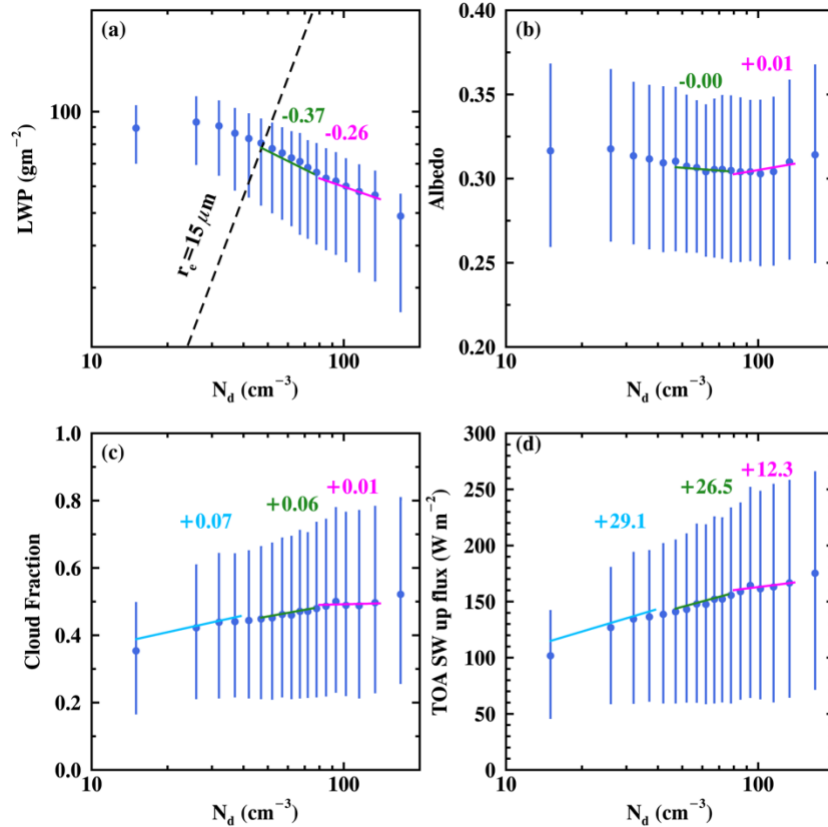
247 Since precipitating and non-precipitating clouds exhibit distinct responses to aerosol perturbations due to
 248 the effect of precipitation suppression and the wet-scavenging feedback, it is critical to distinguish between these
 249 two cloud states when estimating AIE. Previous studies have utilized various methods based on the effective radius
 250 threshold (e.g., Gryspeerd et al., 2019, Toll et al., 2019; Zhang et al., 2022) and the rain rate threshold (e.g., Duong
 251 et al., 2011; Terai et al., 2015) from satellite retrievals. In our study, we validate these two methods using the
 252 precipitating mask estimated from ground-based observations with a radar reflectivity threshold together with the
 253 lidar-defined cloud base at the ARM ENA site (e.g., Wu et al., 2020). The thresholds of $r_e > 12 \mu m$ and $r_e > 15 \mu m$
 254 yield hit rates of 0.79 and 0.73, respectively. However, the false alarm rate is higher for $r_e > 12 \mu m$ (0.21) compared
 255 to $r_e > 15 \mu m$ (0.1). Rain rate is computed using the empirical relationships derived from ground-based
 256 measurements in Comstock et al. (2004) as $R = 0.0156 (LWP/N_d)^{1.75}$. Using a threshold of $R > 0.05$ mm/h results
 257 in a hit rate of 0.65. Consequently, we use the $r_e > 15 \mu m$ threshold to define precipitating clouds in this study.

258 To investigate the dependences of cloud susceptibility on previous cloud states and quantify the influence
259 of cloud memory on the estimated cloud susceptibility, we track the historical cloud state over a $1^\circ \times 1^\circ$ grid box for
260 a two-hour period. During the summer in the study region, low wind conditions prevail in the boundary layer, with
261 the mean wind speed being less than 10 m/s for 85% of the time and less than 7 m/s for 60% of the time. Therefore,
262 in most cases, less than half of the clouds exit the grid box within the two hours, allowing us to track the previous
263 cloud state within the same grid box (i.e., from the Eulerian perspective). The influence of cloud memory is assessed
264 by comparing the cloud susceptibilities of clouds that undergo a transition in cloud state with those that do not
265 experience such a transition. Section 3.4 provides more details and discussion on the sensitivity of tracking time and
266 the influence of advection on our classification.

267 **3. Results**

268 **3.1 General cloud conditions and mean cloud responses to N_d perturbations**

269 In the ENA region, characterized by dominant Bermuda High with its prevailing ridge and zonal synoptic
270 pattern (Mechem et al., 2018), the summer season gives rise to the annual peak in boundary layer cloud coverage
271 The monthly mean low-level CF retrieved from Meteosat-11 reaches its maximum of 35% in July, compared to an
272 annual mean of 17% during the four-year study period. This region represents a typical clean marine condition,
273 situated far from continental influences, which results in a consistently low N_d compared to polluted marine regions,
274 such as the northeastern (NE) Pacific near California or the northwestern Atlantic near the Gulf of Maine. In July,
275 the mean N_d over the ENA region is 65 cm^{-3} with the lower 5th and upper 95th percentile of 15 and 160 cm^{-3} ,
276 respectively. The retrieved N_d values in this study closely align with in-situ measurements from the Aerosol and
277 Cloud Experiments in Eastern North Atlantic (ACE-ENA) field campaign. For instance, the in-situ measured N_d in
278 July 2017 varied from 25 to 150 cm^{-3} , with a mean value of 65 cm^{-3} (e.g., Yeom et al., 2021; Zhang et al., 2021).
279 Moreover, our satellite retrieved N_d exhibits good agreement with retrievals based on ground-based observations at
280 the ARM ENA site (e.g., Dong et al., 2014; Wu et al., 2020) and the MOderate resolution Imaging
281 Spectroradiometer (MODIS, e.g., Bennartz 2007; Bennartz and Rausch 2017).



282
 283 Figure 1. Relationships between N_d and cloud properties: (a) cloud LWP, (b) cloud albedo, (c) cloud fraction, and
 284 (d) TOA shortwave upward radiative flux. The dots represent the mean values, while the whiskers indicate the upper
 285 and lower 25th percentile. In (a), the dashed line denotes $r_e = 15 \mu\text{m}$, serving as an indicator of precipitation
 286 occurrence, with precipitating clouds located to the left of the line. Blue, green, and magenta lines in panels (a)-(d)
 287 represent the regression slopes of the mean cloud properties, and the mean $\ln(N_d)$, for $N_d < 40 \text{ cm}^{-3}$, N_d between
 288 40 and 80 cm^{-3} , and $N_d > 80 \text{ cm}^{-3}$, respectively.

289 Previous studies have demonstrated that clouds exhibit diverse responses to aerosol perturbations under
 290 clean and polluted conditions (e.g., Fan et al. 2016; Mülmenstädt and Feingold, 2018). Figure 1 shows the
 291 relationships between the climate mean cloud properties, derived from the pixel-level SEVIRI cloud products, and
 292 averaged to the $1^\circ \times 1^\circ$ resolution, as a function of the $1^\circ \times 1^\circ$ mean N_d values. To quantify these responses, cloud
 293 susceptibility is estimated as the slope of the mean cloud variable changes across N_d bins. In pristine conditions (N_d
 294 $< 40 \text{ cm}^{-3}$, ~28% of data), clouds predominantly precipitate ($r_e > 15 \mu\text{m}$, Fig.1a). The mean cloud LWP features a
 295 slight increase followed by a decrease with increasing N_d . This result departs from the precipitation suppression
 296 hypothesis, in which LWP typically increases. The absence of a precipitation suppression signal is likely attributed
 297 to the relatively modest precipitation that occurs in this region during summer (e.g., Wu et al., 2020; Zheng and
 298 Miller, 2022), resulting in a minimal precipitation suppression effect and a dominant entrainment drying effect. In
 299 terms of α_c , the potential decrease in α_c attributed to a LWP reduction offsets the potential increases in α_c caused by
 300 the Twomey effect, resulting in a net zero change in mean α_c for clouds with $N_d < 40 \text{ cm}^{-3}$ (Fig.1b). Furthermore,
 301 the majority of precipitating clouds are broken, with a mean CF that increases with N_d from 0.35 to 0.45 (Fig.1c).
 302 Consequently, the mean SW_{TOA}^{up} flux increases from 100 to 140 W m^{-2} as N_d increases from 10 to 40 cm^{-3} . This

303 increase in CF for precipitating clouds aligns with previous study over the north Atlantic region across all seasons
304 (e.g., Gryspeerdt et al., 2016). In summary, despite the slight decrease in mean LWP with increasing N_d for
305 precipitating clouds, the mean cloud albedo remains relatively constant, while the mean CF increases, resulting in an
306 overall increase in the TOA reflected shortwave flux.

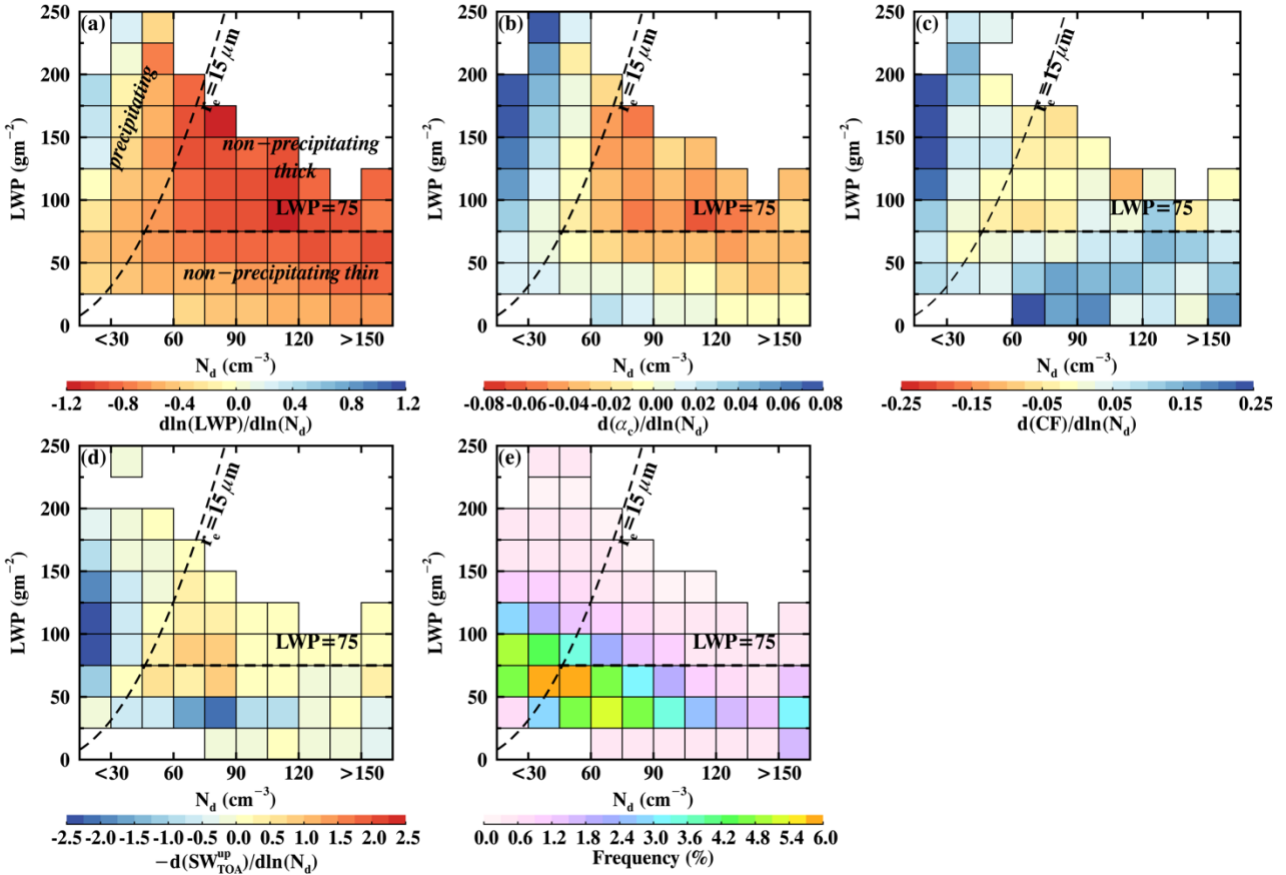
307 Under relatively polluted conditions with $N_d > 40 \text{ cm}^{-3}$ (~72% of data), the mean LWP shows a
308 decreasing trend with N_d . For N_d values between 40-80 cm^{-3} , the $\ln(\text{LWP}) - \ln(N_d)$ slope is -0.37 , while for N_d
309 exceeding 80 cm^{-3} , the slope reaches -0.26 (green and magenta lines in Fig.1a). This negative adjustment of LWP
310 for non-precipitating clouds is consistent with the sedimentation-evaporation-entrainment feedback, as well as with
311 previous studies of stratocumulus clouds in other regions (e.g., Gryspeerdt et al., 2019; Zhang et al., 2022). The
312 mean α_c remains nearly constant within the N_d range of 40-80 cm^{-3} (Fig.1b). As LWP decreases at a slower rate
313 for $N_d > 80 \text{ cm}^{-3}$, the Twomey effect becomes more dominant and leads to a slight increase in α_c with a slope of
314 0.01 (magenta line in Fig.1b). For non-precipitating clouds, the mean CF slightly increases with increasing N_d with
315 a CF susceptibility of 0.06 and 0.01 (green and magenta lines in Fig.1c). As a result, the SW_{TOA}^{up} flux exhibits a
316 weaker susceptibility compared to precipitating clouds (Fig.1d).

317 3.2 Daytime mean cloud susceptibilities in the LWP- N_d space

318 One limitation of the relationships derived from the mean cloud properties with sorted N_d is the
319 confounding effect from meteorological impacts on cloud properties and cloud susceptibilities. As a comparison,
320 Fig.2 shows the mean cloud susceptibility estimated within each half-hourly snapshot's $1^\circ \times 1^\circ$ grid box and
321 averaged in the LWP- N_d parameter space. There are around 72,000-82,000 samples of the 1° cloud susceptibilities
322 in this study. The number of samples for different cloud susceptibilities are slightly different due to the goodness of
323 fit test for each regression. We calculate the mean susceptibilities for LWP- N_d bins with more than 100 cloud
324 susceptibility samples. Blank bins in Fig.2 are bins with less than 100 samples. Figure 2e shows the occurrence
325 frequency of samples for the LWP susceptibility in Fig.2a.

326 With the assumption that the meteorological condition is homogeneous in each grid box, the estimated
327 cloud susceptibilities exhibit much stronger relationships for all cloud variables compared to the climatological
328 mean adjustment rates shown in Fig.1. The disparities between the two methods suggest that meteorological
329 confounders tend to obscure the signal of the AIE over the ENA region. Moreover, the cloud responses for both
330 precipitating and non-precipitating clouds exhibit consistent signs between the half-hourly (Fig.2) and
331 climatological-mean approaches (Fig.1). This consistency is likely attributed to the confined domain (a $10^\circ \times 10^\circ$)
332 and the focus on July in this study, which limit the spatial and temporal covariability between cloud properties and
333 N_d . This consistency also demonstrates that the overall cloud responses to N_d perturbations primarily depend on
334 cloud states (e.g., precipitating conditions and cloud thickness).

335 The dependence of cloud response on cloud state is illustrated in Fig.2. We define three cloud states: (1)
336 *the precipitating clouds* ($r_e > 15 \mu\text{m}$), (2) *the non-precipitating thick clouds* ($r_e < 15 \mu\text{m}$, $LWP > 75 \text{ gm}^{-2}$), and (3)
337 *the non-precipitating thin clouds* ($r_e < 15 \mu\text{m}$, $LWP < 75 \text{ gm}^{-2}$), similar to the definition in Zhang et al. (2022).



338
 339 Figure 2. Mean cloud susceptibilities for different N_d and LWP bins during the daytime. (a) cloud LWP
 340 susceptibility ($d\ln(LWP)/d\ln(N_d)$), (b) cloud albedo susceptibility ($d\alpha_c/d\ln(N_d)$), (c) cloud fraction
 341 susceptibility ($dCF/d\ln(N_d)$), (d) cloud shortwave susceptibility ($-dSW_{TOA}^{up}/d\ln(N_d)$) weighted by the frequency
 342 of occurrence of samples of each bin, and (e) frequency of occurrence of samples in each bin. The dashed lines in
 343 (a)-(e) indicate $r_e = 15 \mu\text{m}$ and $LWP = 75 \text{ gm}^{-2}$, as thresholds for precipitation (precipitating clouds located to the
 344 left of the line) and thick clouds (with $LWP > 75 \text{ gm}^{-2}$). The defined three clouds states are noted in (a).

345 *a. Precipitating clouds*

346 Among warm boundary layer clouds, precipitating clouds are the dominant cloud state in July over the
 347 study region, with a total frequency of occurrence of 46% (Fig.2e). The increase in cloud LWP with increasing N_d is
 348 observed primarily in heavily precipitating thick clouds with $N_d < 30 \text{ cm}^{-3}$ and $LWP > 125 \text{ gm}^{-2}$ (Fig.2a).
 349 However, these clouds occur relatively infrequently at ENA, accounting for only 2% of the total warm boundary
 350 cloud population (Fig.2e). In contrast, most of the precipitating clouds at ENA are lightly precipitating with
 351 $15 < r_e < 20 \mu\text{m}$ (Fig.2e and Fig.S2c) and they exhibit a slight decrease of LWP with N_d (Fig.2a). The mean LWP
 352 susceptibility for lightly precipitating clouds ranges from -0.5 to -0.2 for different bins, with a mean value of -0.4 .
 353 The standard deviations of LWP susceptibility in different LWP- N_d bins vary between 0.4 to 1.2, while the LWP
 354 susceptibilities for precipitating clouds are significantly different than other two cloud states at a 95% confidence
 355 level. The slight decrease in LWP for lightly precipitating clouds aligns with previous findings over the Pacific,
 356 Atlantic, and global oceans for marine stratocumulus (e.g., Fig S4 in Zhang and Feingold, 2023).

357 The contrasting response of LWP to N_d perturbations for lightly and heavily precipitating clouds can be
 358 attributed to the interplay of two competing processes: the depletion of LWP caused by the sedimentation-
 359 evaporation-entrainment feedback and the accumulation of LWP resulting from the precipitation suppression
 360 feedback. Heavily precipitating clouds are predominantly overcast with a mean CF of 0.65 (Fig.S2a) and a mean r_e
 361 of $25 \mu m$ (Fig.S2c). Precipitation acts to stabilize the boundary layer, remove water from cloud top, and reduce the
 362 entrainment rate (Sandu et al., 2007, 2008). Therefore, heavily precipitating clouds exhibit smaller entrainment rate
 363 than non-precipitating clouds with similar LWP. The increase of LWP from precipitating suppression feedback
 364 outweighs the decrease of LWP from entrainment feedback and results in a net increase in LWP (e.g., Chen et al.,
 365 2014; Toll et al., 2019). In lightly precipitating clouds, however, the suppression effect of drizzle on the entrainment
 366 rate is minimal. Therefore, the decrease in LWP from entrainment overpowers the increases in LWP from
 367 precipitating suppression, leading to a net decrease in LWP with increasing N_d (e.g., Xue and Feingold, 2006).

368 Precipitating clouds generally exhibit brighter cloud albedo with increasing N_d as a result of the weak
 369 negative and positive LWP adjustment, particularly in heavily precipitating clouds (Fig.2b). For lightly precipitating
 370 clouds, α_c susceptibilities range from -0.04 to $0.07 \ln(N_d)^{-1}$, with a mean of $0.02 \ln(N_d)^{-1}$. The suppression of
 371 precipitation by N_d also lead to a significant increase in CF for heavily precipitating clouds, with slopes greater than
 372 $0.25 \ln(N_d)^{-1}$. For most of the lightly precipitating clouds, the mean CF exhibits small variation with N_d
 373 perturbations, with CF susceptibilities ranging between $\pm 0.025 \ln(N_d)^{-1}$ (Fig.2c). The standard deviation of the
 374 1° α_c and CF susceptibilities for different precipitating bins ranges between 0.05-0.15 and 0.3-0.6, respectively. The
 375 α_c and CF susceptibilities for precipitating clouds are significantly different than other two cloud states at a 95%
 376 confidence level. Considering the combined effects of increased α_c and CF, the mean radiative response for
 377 precipitating clouds amounts to $-13 W m^{-2} \ln(N_d)^{-1}$, which is a cumulative shortwave susceptibility of bins
 378 classified as precipitating clouds in Fig.2d, weighted by their frequency of occurrence. The contributions from CF
 379 and α_c effects are -9.5 and $-3.5 W m^{-2} \ln(N_d)^{-1}$, respectively (Eq. 3).

380 *b. Non-precipitating thick clouds*

381 Non-precipitating thick clouds are less frequent, the total frequency of occurrence is 10% (Fig.2e). Their
 382 cloud LWP responses to N_d perturbations differ from that of precipitating clouds. The LWP susceptibility for non-
 383 precipitating thick clouds is the most negative among the three cloud states, and it reaches a minimum value of -1.2
 384 at the high-LWP and high- N_d ends (Fig.2a). As LWP and N_d decrease, the LWP susceptibility gradually increases
 385 from -1.2 to -0.6 . This negative susceptibility is likely explained by the evaporation enhancement associated with
 386 smaller droplets at high N_d values (e.g., Xue and Feingold, 2006; Small et al., 2009), which works in concert with an
 387 entrainment strengthening expected in clouds with large LWP (e.g., Sandu et al., 2008, Williams and Igel, 2021). In
 388 addition, clouds with higher N_d and larger LWP exhibit stronger shortwave absorption, which enhance LWP
 389 depletion and therefore a more negative LWP susceptibility (e.g. Bores and Mitchell, 1994; Petters et al. 2012). The
 390 mean LWP susceptibility for non-precipitating thick clouds is -0.94 . Consistent with the negative LWP
 391 susceptibility, non-precipitating thick clouds become less reflective with increasing N_d for all N_d bins with LWP $>$
 392 $75 gm^{-2}$ (Fig.2b). The mean α_c susceptibility is $-0.04 \ln(N_d)^{-1}$. Due to the enhanced entrainment and
 393 evaporation, the mean CF mostly decreases with increasing N_d , with the mean CF susceptibilities ranging from -0.1

394 to $+0.04 \ln(N_d)^{-1}$ (Fig.2c). Considering the decrease in both α_c and CF, non-precipitating thick clouds exhibit a
395 warming effect at the surface, the mean radiative response is $+4.4 W m^{-2} \ln(N_d)^{-1}$ (Fig.2d), with contributions
396 from the albedo effect and the CF effect of 2.9 and $1.5 W m^{-2} \ln(N_d)^{-1}$, respectively.

397 *c. Non-precipitating thin clouds*

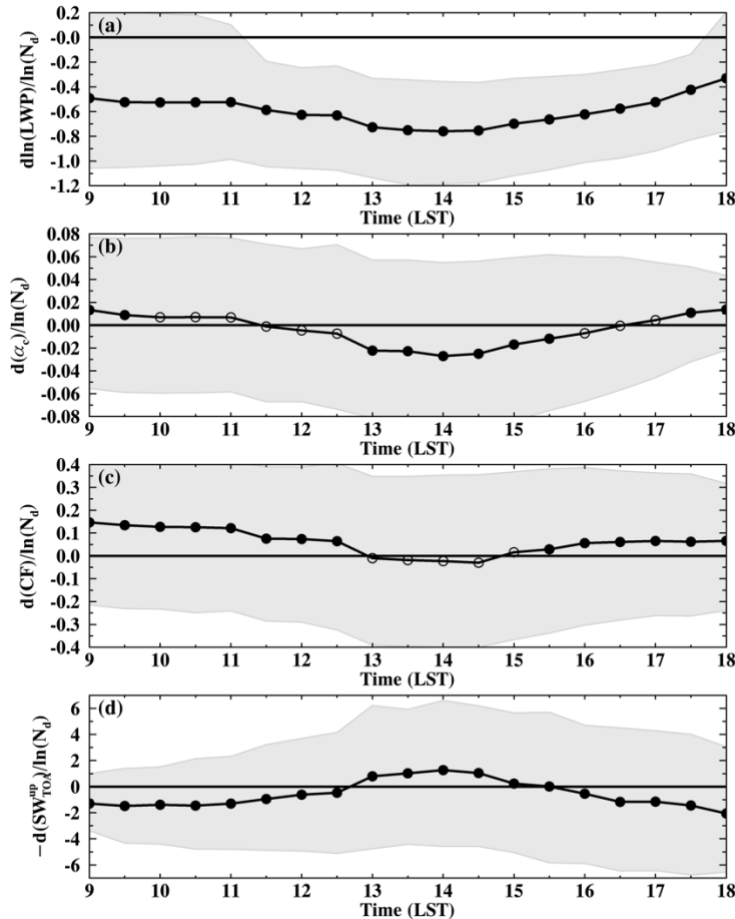
398 Non-precipitating thin clouds are more common than thick clouds during summer, with a total frequency of
399 occurrence of 44% (Fig.2e). Compared to non-precipitating thick clouds, they exhibit consistent negative but
400 slightly weaker LWP responses to N_d perturbations. The mean LWP susceptibilities range from -0.9 to -0.4 in
401 different LWP- N_d bins with a mean of -0.7 (Fig.2a). Similar to non-precipitating thick clouds, non-precipitating
402 thin clouds mostly become darker with increasing N_d . Interestingly, with largely decreased LWP, the mean CF
403 mostly increase for all N_d conditions, the CF susceptibilities range from $+0.02$ to $+0.25 \ln(N_d)^{-1}$ (Fig.2c). The
404 sedimentation- evaporation-entrainment feedback alone cannot explain the opposite signs in in LWP and CF
405 susceptibilities for non-precipitating thin clouds. A possible explanation for the increased CF is that the enhanced
406 cloud top radiative cooling rate from aerosol perturbations help to mix the boundary layer, facilitate moisture
407 transport from the ocean surface to cloud, and therefore favor new cloud formation and extend cloud lifetime (e.g.,
408 Christensen et al. 2020). This hypothesis is consistent with and supported by the relative low CF for these clouds
409 (Fig.S2a) and the diurnal variation in LWP susceptibility for non-precipitating thin clouds, which will be discussed
410 in the next section. The opposite signs of LWP and CF susceptibilities indicate that the AIE might redistribute cloud
411 water horizontally and make the thin clouds thinner and wider. The CF radiative effect from increased CF
412 dominates the albedo effect from darker clouds and lead a net cooling at the surface. The mean radiative response is
413 $-5.2 W m^{-2} \ln(N_d)^{-1}$, with CF and albedo contributions of -8.3 and $+3.1 W m^{-2} \ln(N_d)^{-1}$, respectively (Fig.2d).

414 To sum up, the magnitudes and signs of the responses of cloud LWP, α_c , and CF to N_d perturbations
415 primarily depend on the cloud states. Precipitating clouds mostly become thinner and brighter with increasing N_d ,
416 accompanied by a slight increase in CF. An increase in LWP with increasing N_d is observed only for heavily
417 precipitating clouds with $N_d < 30 cm^{-3}$ and $LWP > 125 gm^{-2}$. Non-precipitating thick clouds become thinner, less
418 reflective, and decrease in cloudiness with N_d perturbations. On the other hand, non-precipitating thin clouds
419 become thinner and less reflective, but their cloudiness increase as N_d increases. Given the dependence of AIE on
420 cloud state, we will apply the cloud state classification in the following two sections with the goal of facilitating a
421 process-level understanding of cloud responses and the daytime variation in cloud susceptibilities.

422 **3.3 Daytime variation of cloud susceptibility**

423 As discussed in the introduction, warm boundary layer clouds exhibit a distinct diurnal cycle in both cloud
424 properties and frequency of occurrence of cloud states during summer. In this section, we investigate the daytime
425 variation of cloud susceptibility from 9 to 18 local standard time (LST) using the half-hourly Meteosat-11 retrievals.
426 The domain mean daytime variation of cloud susceptibility is estimated from each half-hourly time step within each
427 $1^\circ \times 1^\circ$ box and then averaged over the study domain ($33-43^\circ N$, $23-33^\circ W$) during the four months. In the study
428 domain, there is little spatial variability in cloud susceptibilities and the diurnal cycle of the cloud susceptibility for
429 the $1^\circ \times 1^\circ$ box at the ARM ENA site agree well with the domain mean pattern (not shown). Furthermore, diurnal

430 cycle of the cloud microphysical properties (e.g., r_e , τ , LWP, N_d) show little difference between the domain mean
 431 value or that averaged over the $1^\circ \times 1^\circ$ box at the ARM ENA site. The cloud microphysics retrievals from
 432 Meteosat-11 agree well with retrievals based on ground-based radar and lidar observations in the daytime variation
 433 (not shown). Therefore, the ARM ENA site at the Azores archipelago can represent the cloud properties and the AIE
 434 for warm boundary layer clouds over the study region.



435 Figure 3. Daytime variation of cloud susceptibilities. (a) cloud LWP susceptibility ($d\ln(\text{LWP})/d\ln(N_d)$), (b) cloud
 436 albedo susceptibility ($d\alpha_c/d\ln(N_d)$), (c) cloud fraction susceptibility ($d\text{CF}/d\ln(N_d)$), and (d) cloud shortwave
 437 susceptibility ($-d\text{SW}_{\text{TOA}}^{\text{up}}/d\ln(N_d)$). The shaded areas represent the lower and upper 25th percentile of the cloud
 438 susceptibilities for each time step and the solid lines with dots represent the mean values. In (b) and (c), filled
 439 markers indicate data points that susceptibilities are significantly different from zero ($p < 0.05$), while open markers
 440 indicate statistical insignificance.
 441
 442

443 Warm boundary layer clouds witness distinct and significant daytime variations in cloud susceptibilities
 444 (Fig.3). For example, the mean LWP susceptibility exhibits a magnitude of change of 0.4 from morning to evening,
 445 which corresponds to approximately 30-40% of the overall variability in LWP susceptibility (Fig.3a). Similarly, the
 446 α_c and CF susceptibility undergo magnitude of changes of approximately 20-30% compared to the overall
 447 variability (Figs. 3b and c). The high variability in cloud susceptibility highlights the complex synoptic,
 448 meteorological and cloud conditions as well as the interplay between them in the ENA region. Nevertheless, the

449 daytime variation of cloud susceptibility is statistically significant at a 95% confidence level based on a student's t-
450 test. Interestingly, all three cloud variables exhibit a "U-shaped" diurnal cycle in cloud susceptibilities with less
451 negative/more positive values in the morning and evening and more negative values at noon. Additionally, both α_c
452 and CF susceptibilities switch signs from positive in the morning to negative at noon, and then become positive
453 again in the evening. The switch in sign for albedo susceptibility is statistically significant at a 95% confidence
454 level, while the switch in sign for CF susceptibility is not statistically significant (Figs. 3b, c). As both α_c and CF
455 increase with increasing N_d in the morning, AIE has a cooling effect at the surface and the estimated shortwave
456 susceptibility is $-1.4 W m^{-2} \ln(N_d)^{-1}$. During 13-15 LST, the shortwave susceptibility switches sign to a warming
457 effect of $+1.2 W m^{-2} \ln(N_d)^{-1}$ (Fig.3d).

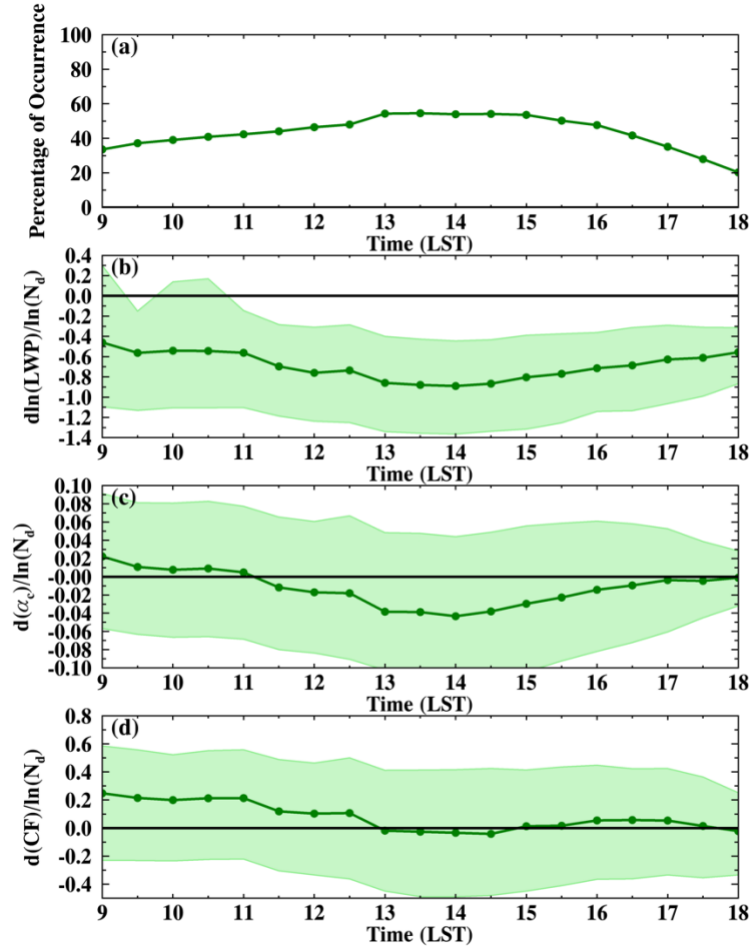
458 Given the pronounced daytime variation of cloud susceptibility, *how can we explain this distinct daytime*
459 *variation, and which state of cloud contributes most to the daytime variation?* One possible explanation is the
460 increased occurrence of precipitating clouds in the morning and evening during summer (Remillard et al, 2012),
461 which increase cloud susceptibility, as depicted in Fig.2. To investigate this hypothesis and quantify the impacts of
462 different cloud states on the variabilities of cloud susceptibilities, we examined the daytime variation of cloud
463 susceptibility, along with the daytime shift in occurrence frequency for each cloud state.

464 **3.4 Daytime variation of cloud susceptibility for different cloud states**

465 **3.4.1 Non-precipitating thin clouds**

466 Non-precipitating clouds mainly consist of thin clouds, with a daytime mean occurrence of 44% (Fig.4a).
467 The highest occurrence is observed around noon, which is consistent with ground-based radar reflectivity
468 measurement at the ENA site (Remillard et al, 2012). Furthermore, as seen in Fig.4, not only the frequency of cloud
469 occurrence, but also the susceptibilities of LWP, α_c , and CF show distinct daytime fluctuations. For example, the
470 mean LWP susceptibility decreases from -0.4 to -0.9 , and the mean α_c susceptibility decreases from 0.02 to -0.04
471 $\ln(N_d)^{-1}$ from morning to noon, followed by increases in both LWP and α_c susceptibilities in the afternoon. The
472 CF susceptibility is highly positive in the morning and decreases to near zero after 13 LST. In addition, cloud
473 susceptibility for thin clouds in the morning is statistically significantly different from that at noon and in the
474 evening at a 95% confidence level.

475



476
 477 Figure 4. Daytime variation of (a) percentage of occurrence of non-precipitating thin clouds to warm boundary layer
 478 clouds, (b) cloud LWP susceptibility ($d\ln(LWP)/d\ln(N_d)$), (c) cloud albedo susceptibility ($d\alpha_c/d\ln(N_d)$), and (d)
 479 cloud fraction susceptibility ($dCF/d\ln(N_d)$) for non-precipitating thin clouds. The shaded areas represent the lower
 480 and upper 25th percentile of the cloud susceptibilities for each time step and the solid lines with dots represent the
 481 mean values.

482 To explain the decrease of cloud susceptibility of non-precipitating thin clouds from morning to noon, we
 483 test two hypotheses (H1 and H2 in Table 1). Hypothesis H2 is related to the dissipation of thin clouds during this
 484 period, which is caused by a decreased LWP due to increased solar radiation. During the dissipation, both LWP and
 485 r_e decrease. As r_e is raised to the power of $-\frac{5}{2}$ in Eq. (1) compared to τ being raised only to the power of $\frac{1}{2}$, the
 486 decreases of LWP and r_e could still result in an increase in the retrieved N_d . Consequently, a LWP decrease and N_d
 487 increase lead to a decrease in LWP susceptibility during the dissipation (Gryspeerdt et al., 2019). To examine this
 488 hypothesis (H2), non-precipitating thin clouds are classified as: growing, dissipating, or constant based on the
 489 changes in the mean CF, cloud susceptibilities for the three groups are shown in Fig.S3. More specifically, we
 490 calculate the change in the mean CF within a 30-minute window for each fixed $1^\circ \times 1^\circ$ box. If the mean CF increase
 491 (decrease) more than 10%, clouds are classified as growing (dissipating). If the change in CF is less than 10%,
 492 clouds are classified as constant. Similar results are obtained using classification methods based on different CF
 493 thresholds (e.g., from 10% to 30%), and during different time windows from 30-minutes to two hours (not shown).

494
495

Table 1. List of hypotheses and associated explanations for the daytime variation of LWP and CF susceptibilities for different cloud states.

	Cloud state	Hypotheses:	
Daytime evolution of LWP susceptibility	Non-precipitating thin clouds	H1*:	Non-precipitating thick clouds transition to thin clouds from morning to noon, which leads to a daily minimum LWP susceptibility at noon.
		H2*:	Cannot explain. Clouds that are growing or dissipating have similar LWP susceptibilities as clouds with constant CF.
	Non-precipitating thick clouds	H1:	Thin clouds develop to thick clouds from noon to evening, which leads to an increase in LWP susceptibility.
		H2:	Cannot explain.
	Precipitating clouds	H1:	Non-precipitating thin clouds transition to precipitating clouds in the afternoon, which leads to a decrease in LWP susceptibility.
		H2:	Cannot explain.
Daytime evolution of CF susceptibility	Non-precipitating thin clouds	H1:	Thick clouds transitioned to thin clouds from morning to noon, leading to a decrease in CF susceptibility
		H2:	Cannot explain.
	Non-precipitating thick clouds	H1:	Cannot explain.
		H2:	Cannot explain.
		H3*:	Mostly overcast clouds in the morning and evening. CF of overcast clouds is less sensitive to N_d perturbations.
	Precipitating clouds	H1:	Thin clouds transition to precipitating clouds in the afternoon, and lead to a decrease in CF susceptibility
		H2:	Cannot explain.

496 *H1: LWP and CF responses to N_d perturbations slower than the transition of cloud state.

497 *H2: Dissipation or development of clouds.

498 *H3: Changes in cloud morphology.

499 As seen in Fig. S3b, the LWP susceptibilities for non-precipitating thin clouds in the growing or dissipating
500 stages are similar or less negative than clouds that remain constant in CF, which contradicts the hypothesis H2.
501 Additionally, the occurrence of dissipating and developing thin clouds remain relatively constant throughout the day
502 (Fig.S3a), which differs from our hypothesis that thin clouds dissipate in the morning. Therefore, the decrease in
503 LWP susceptibility in the morning is *unlikely* to be attributed to the dissipation or development of thin clouds. Yet,
504 due to the observational limitation on estimating the mixing process from satellite retrievals, further investigation is
505 needed to quantify the impact of cloud dissipation on the N_d -LWP relationship.

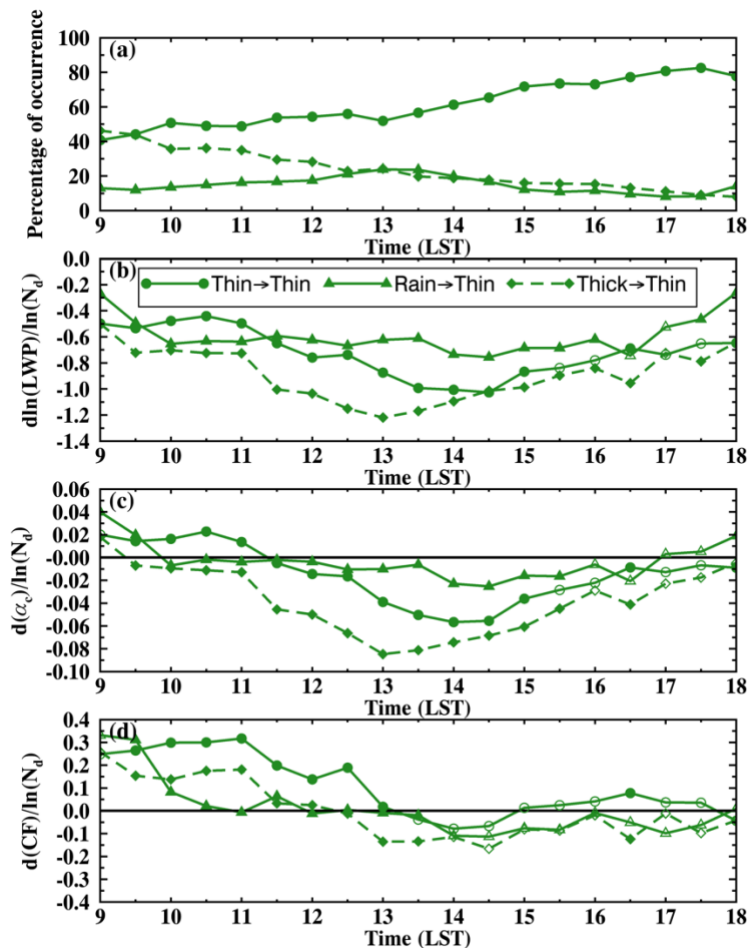
506 Besides the change in CF, dissipation/development of clouds can be defined by change in LWP. However,
507 as our definition of thin and thick clouds use LWP thresholds, results based on change in LWP are similar to results
508 shown in Fig.5, but with weaker signal (not shown). This indicates that classification of precipitating versus non-
509 precipitating clouds is necessary in distinguishing cloud responses to N_d perturbations rather than merely using the
510 LWP threshold.

511 Hypothesis H1 is related to the response time of cloud LWP and CF to N_d perturbations. Both numerical
512 models and observations have shown that the influence of aerosols on cloud LWP, achieved through adjusting the
513 entrainment rate, may take four hours to become apparent and up to 20 hours to reach an equilibrium (e.g.,
514 Glassmeier et al. 2021; Gryspeerdt et al., 2021; Fons et al., 2023). Similarly, CF increases gradually from increasing
515 aerosols and may take approximately three to four hours to reach its maximum effect after the initial perturbation
516 (Gryspeerdt et al., 2021). Therefore, we hypothesize that if clouds change state during the adjustment time, clouds
517 may still retain the “memory” of their responses to N_d perturbations from the previous state. The possible physical
518 processes and mechanisms for this hypothesis is that the LWP susceptibility is mainly driven by cloud top
519 evaporation and entrainment rate. The positive feedback among entrainment, evaporative cooling, long-wave
520 radiative cooling, and mixing from cloud top form a positive feedback loop and set up an environment conducive to
521 enhanced entrainment and evaporation. These feedback and environment will not change immediately even when
522 the cloud LWP decrease and cloud transition to a thin state or vice versa. With the diurnal variation in cloud
523 properties and transition in cloud state, it leads to a diurnal evolution in cloud susceptibility.

524 To quantify the dependence of current cloud susceptibility on previous cloud states, we track the cloud state
525 for each $1^\circ \times 1^\circ$ box backward in time for two hours and classify the non-precipitating thin clouds into three groups
526 (Fig.5): (1) thin clouds that are currently classified as thin clouds and didn't change states in the past two hours (thin
527 \rightarrow thin), (2) thin clouds that evolved from precipitating clouds (rain \rightarrow thin), and (3) thin clouds that decayed from
528 non-precipitating thick clouds (thick \rightarrow thin). This backward tracking classification is applied at each time step. As
529 shown in Fig.5a, at 9 LST, ~50% of the non-precipitating thin clouds originate from thick clouds in previous hours.
530 The transition from thick to thin clouds is likely caused by the increased solar radiation after sunrise, leading to
531 cloud turbulent decoupling from the ocean surface and a decrease in cloud LWP. In the evening, on the other hand,
532 around 80% of the thin clouds are thin clouds in previous hours. In addition, less than 20% of the non-precipitating
533 thin clouds transition from precipitating clouds.

534 In consistent with our hypothesis, non-precipitating thin clouds that are previously thick have significantly
535 more negative LWP and α_c susceptibilities than thin clouds that are previously thin or precipitating (Figs. 5b and c).
536 The differences between the two categories are most pronounced from late morning to early afternoon and less
537 pronounced in the early morning and evening. Such pattern is likely attributed to the daytime evolution of marine
538 boundary layer and cloud coupling state. For example, in the early morning (e.g., 9-10 LST), even with higher
539 frequency of occurrence of thick clouds transitioning to thin clouds, the LWP susceptibility for the thick-to-thin
540 category is less negative compared to later time (dashed line with diamond symbols in Figs 5a, b). This is attributed
541 to the less negative LWP susceptibility for non-precipitating thick clouds in earlier time (e.g., 7-9 LST, not shown),
542 in connection with a well-mixed boundary layer able to transport moisture from the ocean to the cloud, which
543 compensates the moisture loss from aerosol-enhanced entrainment (e.g., Sandu et al., 2008), so that both thick and
544 thin clouds exhibit less negative LWP susceptibilities. From late morning to early afternoon, with increasing solar
545 radiation, deepening of boundary layer and clouds decoupled from surface, LWP susceptibility for thick clouds
546 largely decreases and reaches a daily minimum, which contributes to the largest difference between the thin-to-thin
547 and thick-to-thin categories shown in Fig.5b. The opposite processes occur from afternoon to evening, LWP of thick

548 clouds become less susceptible to N_d perturbations, and the difference between the two categories is less
 549 pronounced. These results support our hypothesis that clouds retain the memory of their responses to N_d
 550 perturbations from their previous states.



551 Figure 5. Daytime variation of non-precipitating thin clouds transition from non-precipitating thin clouds (thin →
 552 thin, solid line with circle symbols), precipitating clouds (rain → thin, solid line with triangle symbols), and non-
 553 precipitating thick clouds (thick → thin, dashed line with diamond symbols) in previous two hours. Symbols for
 554 different state transitions are noted in (b). In (b)-(d), filled markers indicate data points that are significantly
 555 different from the other two groups ($p < 0.05$), while open markers indicate statistical insignificance.
 556

557 Similar to LWP, responses of CF to N_d perturbations in the morning retain the memory of the previous
 558 state of clouds. As seen in Figure 5d, thin clouds that transitioned from thick clouds or precipitating clouds have
 559 significantly less positive CF susceptibility than thin clouds that were previously thin, particularly in the morning.
 560 As the CF susceptibility for thin clouds that evolved from precipitating and thick clouds greatly decrease from
 561 morning to noon, the CF susceptibility for thin clouds decrease from large positive to near zero from morning to
 562 noon (Fig.4c). A maximum in CF susceptibility in the early morning is likely associated with the influence of
 563 aerosols on boundary layer mixing and the evolution of boundary layer from morning to noon. The enhanced
 564 entrainment rate and radiative cooling rate from N_d perturbations help to destabilize the boundary layer and
 565 transport moisture from the ocean surface to clouds, facilitating new cloud formation (e.g., Christensen et al. 2020).
 566 As the boundary layer is typically well mixed in the morning with clouds coupled to the surface, the impact of

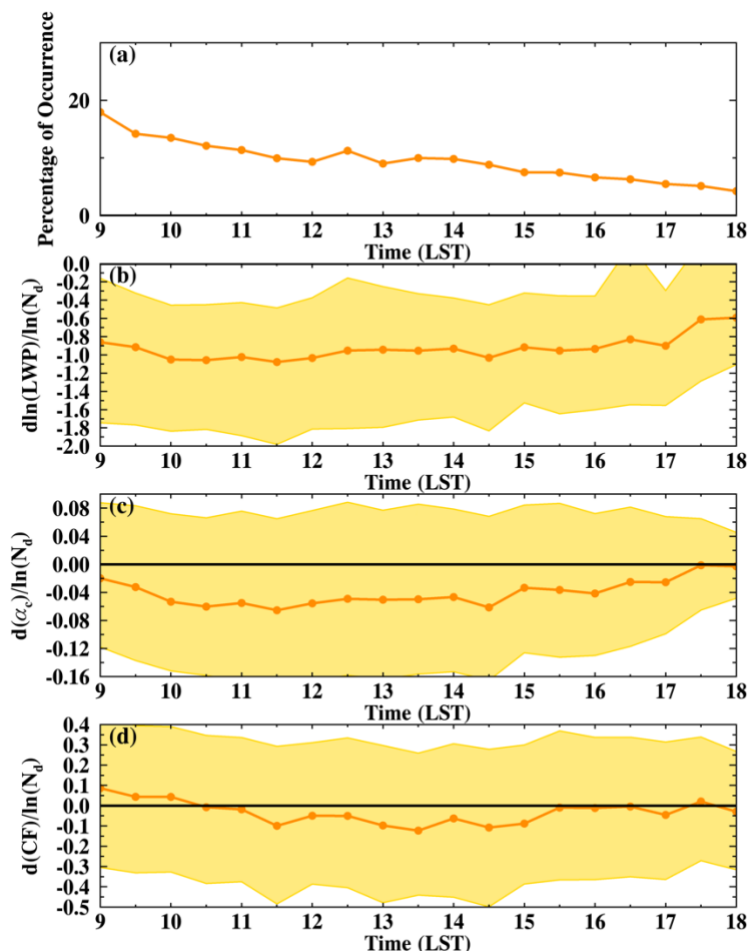
567 aerosols on CF is strongest in the morning and gradually decrease from morning to noon. In the afternoon, thin
568 clouds transition from all three states have near-zero CF responses to N_d perturbations. Further analyses and model
569 simulations are needed to better understand the impacts of aerosols and the associated diurnal evolution of
570 entrainment rate, boundary layer mixing on cloud cover and lifetime, to better explain the observed daytime
571 variation of CF susceptibility for non-precipitating thin clouds.

572 Lastly, the impact of the cloud memory of AIE on current cloud susceptibility is also evident within a 30-
573 minute window when a transition of cloud state just occurs (Fig.S4). Consistent with the findings in Fig.5, thin
574 clouds that transition from thick clouds exhibit much more negative LWP and α_c susceptibilities compared to thin
575 clouds that remain thin during the 30 minutes. Yet, the number of cases experiencing a transition in cloud state
576 within a 30-minute window is limited (Fig.S4a). In addition, the impact of the transition in cloud state on the
577 current cloud susceptibility persists for at least four hours (Fig.S5). As our tracking method does not follow
578 individual cloud parcels to track changes in their states, the influence of cloud advection may become significant
579 over longer tracking time, such as four hours. Therefore, a two-hour tracking window is used in this study.

580 As discussed in the method section, while the advective effects in our study are expected to be modest, we
581 further isolate their impact, by performing an analysis for cloud scenes with wind speed of less than 7 m/s (60% of
582 time), when clouds are somewhat stationary in two hours. Influence of transition in cloud state is consistent as in
583 Fig.5 with more negative LWP and α_c susceptibilities for thin clouds transitioned from thick clouds, while the signal
584 is slightly stronger (not shown). This consistency confirms that our tracking method can capture the signal of cloud
585 state transition and its impact on cloud susceptibilities during summer in the study region.

586 In summary, the “U-shaped” daytime variations in LWP and α_c susceptibilities for non-precipitating thin
587 clouds are likely due to cloud retaining the memory of AIE. From morning to noon, as non-precipitating thick
588 clouds evolve to thin clouds, they retain their memory of the large negative LWP susceptibility. Therefore, both
589 LWP and α_c susceptibilities decrease from morning to noon for thin clouds and reach their daily minima at noon. In
590 the afternoon, as a growing percentage of thin clouds persist as thin clouds during the next hours, LWP and α_c
591 susceptibilities gradually increase to less negative and near zero, respectively.

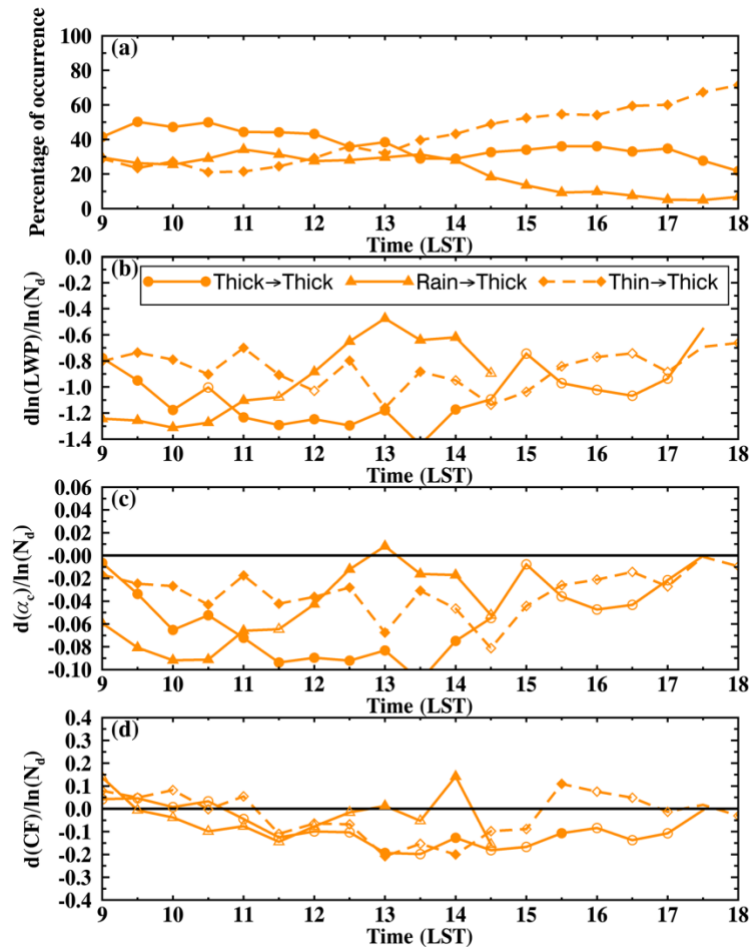
592 3.4.2 Non-precipitating thick clouds



593 Figure 6. Daytime variation of (a) percentage of occurrence of non-precipitating thick clouds to warm boundary
 594 layer clouds, (b) cloud LWP susceptibility ($d\ln(LWP)/d\ln(N_d)$), (c) cloud albedo susceptibility ($d\alpha_c/d\ln(N_d)$),
 595 and (d) cloud fraction susceptibility ($dCF/d\ln(N_d)$) for non-precipitating thick clouds. The shaded areas represent
 596 the lower and upper 25th percentile of the cloud susceptibilities for each time step and the solid lines with dots
 597 represent the mean values.

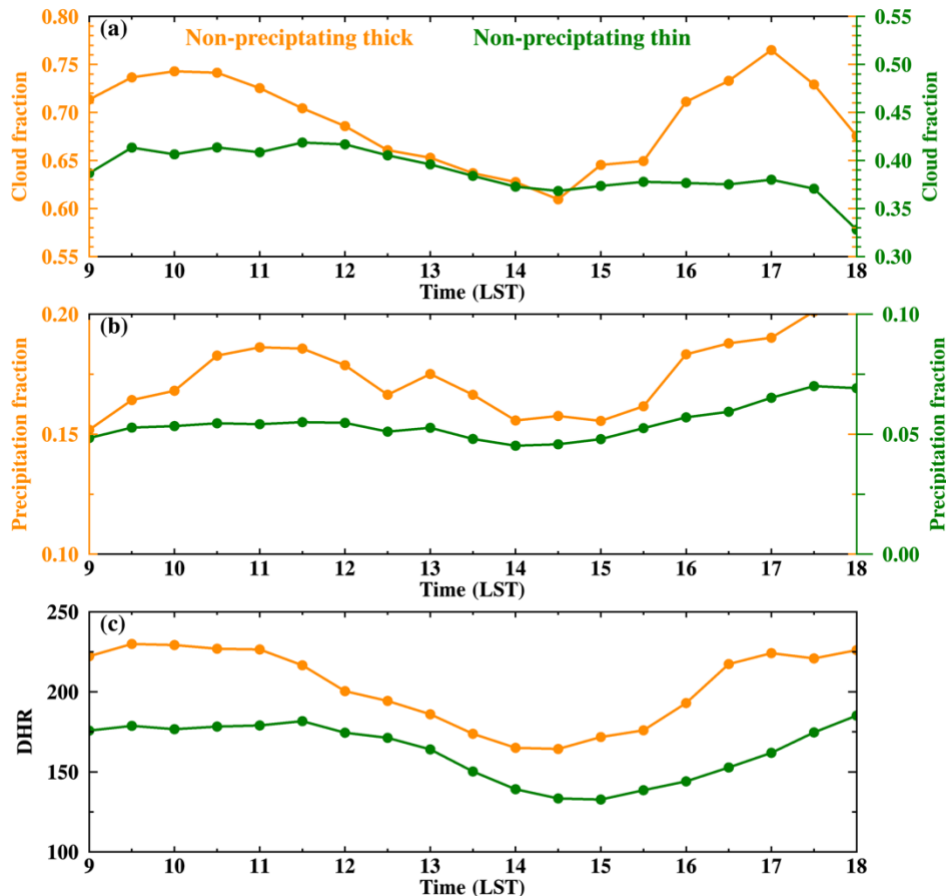
599 Consistent with Fig.2e, non-precipitating thick clouds are the least frequent warm boundary layer cloud
 600 state during summer over the ENA region. Their percentage of occurrence continuously decreases from 20% in the
 601 morning to less than 5% in the evening (Fig.6a). For LWP and α_c , their susceptibilities first decrease from less
 602 negative to more negative in the morning and then increase from noon to evening (Fig.6b and c, respectively). CF
 603 susceptibility is weakly positive in the early morning, becomes weakly negative from late morning to early
 604 afternoon, and increases to near zero in the evening (Fig.6d). The daytime evolutions of LWP and α_c susceptibilities
 605 for thick clouds exhibit consistent trend with cloud susceptibilities for thin clouds transition from thick clouds
 606 shown in Fig.5 but with a lag of two hours. For example, the LWP susceptibility for thick clouds decreases from
 607 -0.8 to -1.1 from 9 to 11 LST and it increase from -1.1 to -0.8 from 11 to 16 LST; while the LWP susceptibility
 608 for the thick-to-thin category in Fig.5b decreases from -0.8 to -1.2 from 11-13 LST and increases to -0.6 from 13
 609 to 18 LST. This result supports our hypothesis on cloud retaining its memory of AIE of its previous cloud state.

610 To gain insight into the observed evolution of LWP and α_c susceptibility from morning to evening, we
 611 investigate the influence of cloud state transition on cloud susceptibility for non-precipitating thick clouds, which is
 612 summarized as H1 in Table 1. As shown in Fig.7a, around 40% of thick clouds sustain as thick clouds from the
 613 previous two hours in the morning; whereas during the late afternoon to evening, with decreasing solar radiation,
 614 more than 60% of thick clouds are developed from thin clouds. Consistent with the findings presented in Fig.5, thick
 615 clouds that are previously thick exhibit significantly more negative LWP susceptibility compared to thick clouds that
 616 are previously thin (Fig.7b). These differences are particularly prominent from late morning to noon and become
 617 insignificant in the afternoon. As discussed before, difference between the thick-to-thick and the thin-to-thick
 618 categories are due to the LWP susceptibilities for thick and thin clouds of previous time, while the smaller
 619 differences in the early morning and afternoon could be attributed to the expected stronger turbulence and cloud
 620 coupling at these times. Additionally, Fig.7d indicates that transition in cloud state cannot explain the daytime
 621 variation in CF susceptibility for thick clouds, as all three groups are insignificantly different from each other.



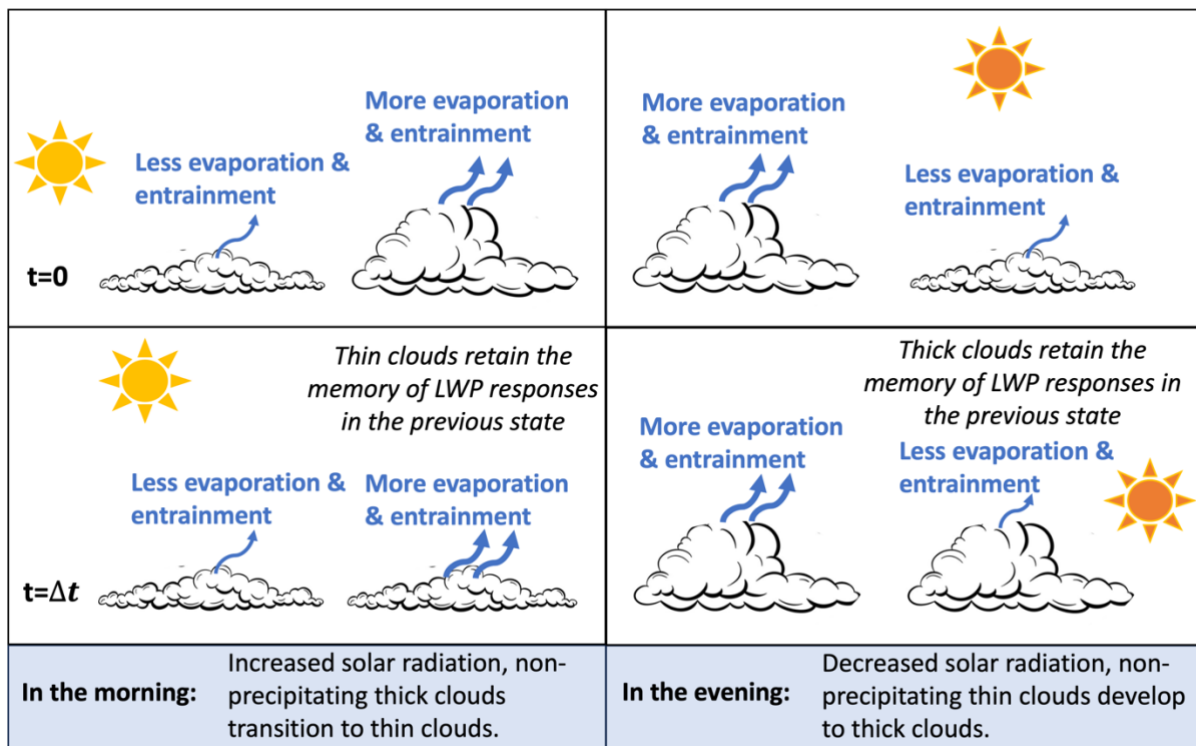
622 Figure 7. Daytime variation of non-precipitating thick clouds transition from non-precipitating thick clouds (thick →
 623 thick, solid line with circle symbols), precipitating clouds (rain → thick, solid line with triangle symbols), and non-
 624 precipitating thin clouds (thin → thick, dash line with diamond symbols) in previous two hours. Symbols for
 625 different state transitions are noted in (b). In (b)-(d), filled markers indicate data points that are significantly
 626 different from the other two groups ($p < 0.05$), while open markers indicate statistical insignificance.
 627

628 To understand the driving mechanism for the daytime variation in CF susceptibility shown in Figure 6d, we
 629 calculate the mean cloud properties for non-precipitating thin and thick clouds, as shown in Fig.8. In the morning,
 630 non-precipitating thick clouds are predominantly overcast clouds with a mean CF of 75% (Fig.8a). To distinguish
 631 between overcast and broken clouds, we calculate the diameter-to-height ratio (DHR) for each cloud, where
 632 diameter is estimated by the square root of the area and height is defined as the 90th percentile of cloud tops. As
 633 shown in Fig.8c, thick clouds are mostly overcast in the morning with a mean DHR of 230. Compared to broken
 634 clouds, overcast clouds have less room for CF to increase, which results in a less positive CF susceptibility for thick
 635 clouds compare to thin. After 10 am, non-precipitating thick clouds start to break. The mean CF decreases from 75%
 636 at 10 am to 60% at 2 pm and the DHR decreases from 230 to 170. As CF for broken clouds is more sensitive to N_d
 637 perturbations, CF susceptibility decreases to $-0.13 \ln(N_d)^{-1}$, which is consistent with the daytime mean negative
 638 CF susceptibility shown in Fig.2c. From afternoon to evening, clouds transition to overcast again (Fig.8), and the CF
 639 susceptibility increases back to zero. This impact of cloud morphology (e.g., overcast or broken clouds) on daytime
 640 variation of CF susceptibility is summarized as H3 in Table 1.



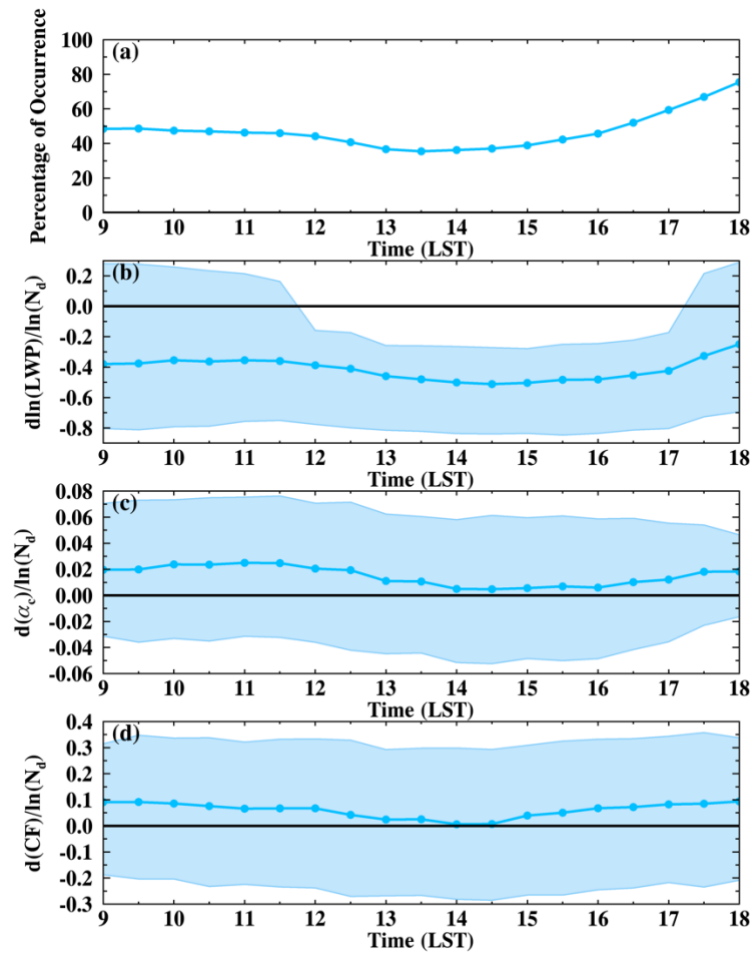
641 Figure 8. Diurnal variation of (a) cloud fraction, (b) pixel-level precipitation fraction, and (c) diameter-to-height
 642 ratio (DHR) for non-precipitating clouds. Different colors represent different cloud states as indicated in (a). Please
 643 note that the non-precipitating thin cloud in (a) and (b) use the y-axis on the right side.
 644

645 The previous results are summarized as follows: LWP susceptibility for non-precipitating thick clouds first
 646 decreases from less negative to more negative in the morning and then increase from noon to evening, which is
 647 likely attributed to the transition from thin to thick clouds. In the morning, 40% to 50% of thick clouds are
 648 previously thick clouds, these clouds exhibit a large negative LWP susceptibility. In the afternoon, with increasing
 649 percentage of thick clouds develop from thin clouds and retain the memory of LWP responses to N_d perturbations of
 650 the thin clouds. LWP susceptibility gradually increases and becomes similar to that of thin clouds (Fig.4b, 6b).
 651 Daytime variation in CF susceptibility for thick clouds is likely attributed to changes in cloud morphology. In the
 652 morning and evening, thick clouds are mostly overcast with CF less sensitive to N_d perturbations, resulting in a near
 653 zero CF susceptibility. From late morning to early afternoon, the overcast thick clouds break down and CF decrease
 654 with increasing N_d likely due to the increased shortwave absorption, the enhanced entrainment, and evaporation.
 655 The impact of cloud memory and transition of cloud state on the daytime variation of LWP susceptibility is
 656 summarized as a schematic figure shown in Fig.9. From morning to noon, as non-precipitating thick clouds
 657 transition to thin clouds, thin clouds retain their memory of AIE of their previous state. Therefore, LWP
 658 susceptibility for thin clouds decreases from morning to noon and reach its daily minima in the early afternoon.
 659 From early afternoon to evening, with non-precipitating thin clouds developing to thick clouds, LWP susceptibility
 660 for thick clouds increase.



661
 662 Figure 9. Schematic figure of influence of cloud memory and transition of cloud state on the LWP susceptibility and
 663 its daytime variation.

664 3.4.3 Precipitating clouds



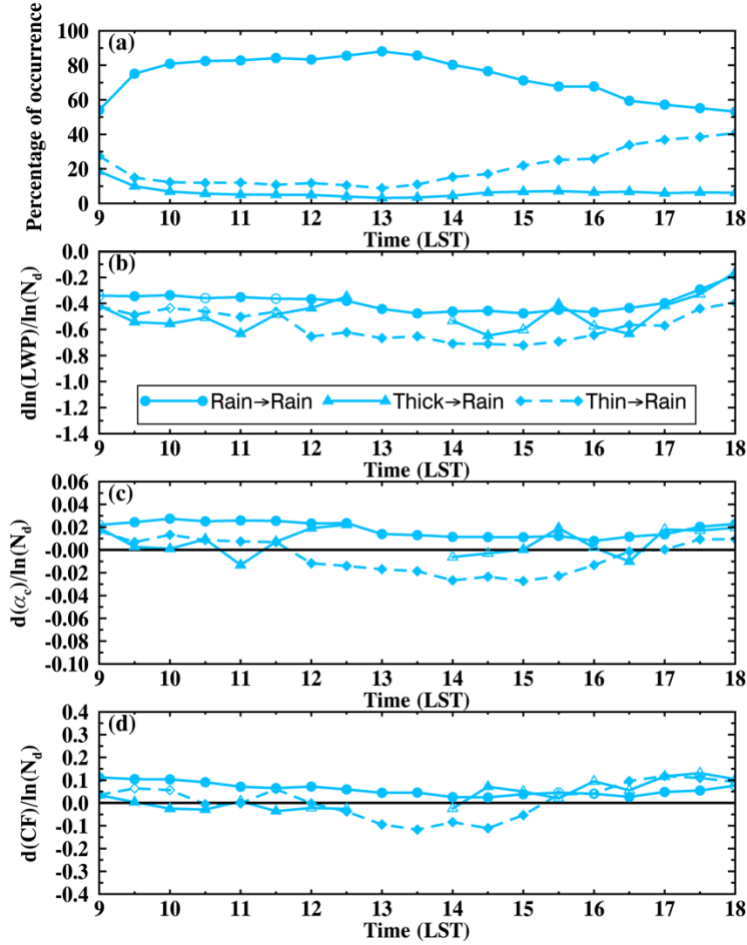
665 Figure 10. Daytime variation of (a) percentage of occurrence of precipitating clouds to warm boundary layer clouds,
 666 (b) cloud LWP susceptibility ($d\ln(LWP)/d\ln(N_d)$), (c) cloud albedo susceptibility ($d\alpha_c/d\ln(N_d)$), and (d) cloud
 668 fraction susceptibility ($dCF/d\ln(N_d)$) for precipitating clouds. The shaded areas represent the lower and upper 25th
 669 percentile of the cloud susceptibilities for each time step.

670 Precipitating clouds, depicted in Figs.10a, are the dominant cloud state in this region, accounting for 46%
 671 of the warm boundary layer clouds, compared to 44% of non-precipitating thin clouds. The frequency of
 672 precipitating clouds is higher in the morning and evening compared to noon. Throughout the day, the mean LWP
 673 susceptibility remain consistently negative, fluctuating between -0.5 to -0.3 , with minimum values between 14–16
 674 LST (Figs.10b). The daytime variability in LWP susceptibility for precipitating clouds is much lower than that for
 675 non-precipitating thin (e.g., from -0.9 to -0.4) and thick (e.g., from -1.1 to -0.6) clouds. The negative LWP
 676 susceptibility is likely due to the prevalence of lightly precipitating clouds, with a mean precipitating fraction
 677 ranging from 0.2 to 0.5 (Fig.S2d). The influence of precipitation suppression is smaller than that of the entrainment
 678 enhancement. Similarly, α_c susceptibility fluctuates between 0 to 0.02 throughout the day, with near zero α_c
 679 susceptibility in early afternoon (Figs.10c). Despite the minimal daytime variation, the LWP and α_c susceptibilities
 680 at 13-16 LST are statistically significant different from cloud susceptibilities in the morning and evening at 95%

681 confidence level with the two-tailed t-test. The CF susceptibility for precipitating clouds also shows minimal
682 daytime variation compared to non-precipitating clouds, with a mean value ranging from 0 to 0.1 (Figs.10d).

683 Consistent with non-precipitating clouds, the daytime variation of LWP and α_c susceptibilities for
684 precipitating clouds can be attributed to the transition of cloud states. For example, as shown in Figs.11b-d,
685 precipitating clouds that transition from non-precipitating thin clouds exhibit significantly more negative/less
686 positive cloud susceptibilities than precipitating clouds that are previously precipitating. Meanwhile, α_c and CF
687 susceptibilities switch signs from positive to negative in the afternoon for precipitating clouds transition from non-
688 precipitating thin clouds compared to that are previously precipitating (dash line with diamond symbols in Figs. 11c,
689 d). Starting from 13 LST, when non-precipitating thin clouds transition to precipitating clouds (Fig.11a), LWP and
690 α_c susceptibilities begin to decrease and reach their daily minimum in the late afternoon. Interestingly, as non-
691 precipitating clouds transition to precipitating clouds (Figs.11b and c, thin \rightarrow rain, thick \rightarrow rain), their LWP and α_c
692 susceptibilities exhibit both less negative values and smaller daytime variations compared to thin/thick clouds that
693 remain as thin/thick (Figs. 5b and c, thin \rightarrow thin, Figs. 7b and c, thick \rightarrow thick). The underlying reason for this
694 observation is currently unclear and warrants further investigation on the sensitivity of AIE for clouds experiencing
695 transition in cloud states, especially between precipitating and non-precipitating clouds. Lastly, the percentage of
696 precipitating clouds that transition from non-precipitating thick clouds is less than 7% (Fig.11a).

697 In conclusion, precipitating clouds exhibit smaller daytime variation in cloud susceptibilities compared to
698 non-precipitating thin and thick clouds. The decrease of LWP and α_c susceptibilities for precipitating clouds in the
699 afternoon is likely contributed by the transition of non-precipitating thin clouds to precipitating clouds.



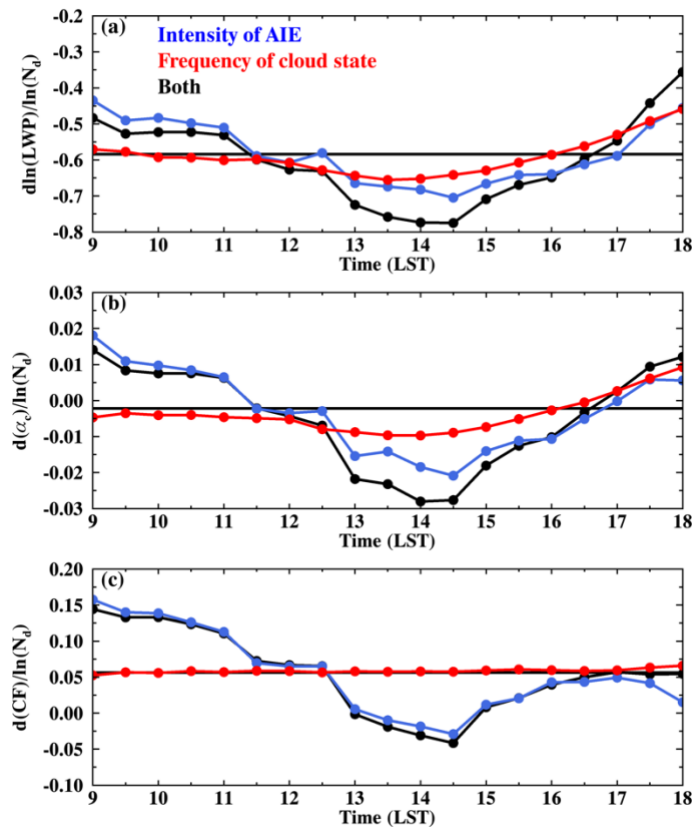
700
 701 Figure 11. Daytime variation of precipitating clouds transitioned from precipitating clouds (rain \rightarrow rain, solid line
 702 with circle symbols), non-precipitating thick clouds (thick \rightarrow rain, solid line with triangle symbols), and non-
 703 precipitating thin clouds (thin \rightarrow rain, dash line with diamond symbols) in previous two hours. Symbols for different
 704 state transitions are noted in (b). In (b)-(d), filled markers indicate data points that are significantly different from
 705 the other two groups ($p < 0.05$), while open markers indicate statistical insignificance.

706 Combining the results shown here and results in section 3.4.1, we can answer which cloud state contributes
 707 the most to the daytime variation of cloud susceptibility. The non-precipitating thin clouds exhibit similar daytime
 708 variations in LWP, α_c , and CF susceptibility than the warm boundary layer clouds (Fig.4 vs. Fig.3), with clouds
 709 being less susceptible to N_d perturbations in the morning and evening and more susceptible at noon. Additionally,
 710 non-precipitating thin clouds have highest frequency at noon. On the other hand, precipitating clouds, despite their
 711 higher percentage of occurrence than thin clouds, exhibit minimal daytime variation in cloud susceptibility.
 712 Therefore, the pronounced daytime variations in cloud susceptibilities for warm boundary layer clouds primarily
 713 stem from non-precipitating thin clouds. The distinct daytime evolution patterns for the three clouds states highlight
 714 the importance of cloud state classification in quantification of cloud susceptibility.

715 3.5 Contribution to the daytime variation of cloud susceptibility

716 As discussed in the previous section, both the frequency of occurrence of cloud states and the intensity of
 717 cloud responses to N_d perturbations exhibit pronounced daytime variations. In this section, we aim to compare the

718 contribution of these two components to the overall daytime variation in cloud susceptibilities by fixing one
 719 component constant at a time. The contribution from changes in the frequency of cloud states is represented by the
 720 red lines in Fig.12, which is estimated by weighting the daytime mean cloud susceptibility (Figs. 2a-c) with the half-
 721 hourly frequency of occurrence of clouds in the LWP- N_d parameter space, assuming a constant intensity of cloud
 722 susceptibility during the daytime. The contribution from changes in the intensity of cloud susceptibility is depicted
 723 by the blue lines, which is estimated by weighting the half-hourly cloud susceptibility in the LWP- N_d parameter
 724 space with the daytime mean frequency of occurrence of clouds (Fig.2e), assuming a constant frequency during the
 725 daytime. The black line in Fig.12 represents the observed susceptibility shown in Fig.3, and it includes the
 726 contributions from daytime variations in both components.



727
 728 Figure 12. Daytime variation in cloud susceptibility contributed from the variability in the intensity of susceptibility
 729 (blue lines with symbols), variability in the frequency of occurrence of cloud state (red lines with symbols), and
 730 from both (black lines with symbols). (a) cloud LWP susceptibility ($d\ln(LWP)/d\ln(N_d)$), (b) cloud albedo
 731 susceptibility ($d\alpha_c/d\ln(N_d)$), (c) cloud fraction susceptibility ($dCF/d\ln(N_d)$). The horizontal black solid lines in
 732 (a)-(c) are the daytime mean susceptibility.

733 When comparing the net observed daytime variation of cloud susceptibilities (black lines) with the
 734 contributions from changes in the intensity and the frequency of cloud state (blue and red lines, respectively), we
 735 find that the daytime changes in cloud susceptibility is primarily driven by changes in the intensity of cloud
 736 susceptibilities during the day. Additionally, as shown in Figs. 12a and b, the red lines are close to the daytime mean
 737 values in the morning, which indicates that variations in the frequency of different cloud states have minimal impact
 738 on changes in LWP and α_c susceptibilities in the morning. On the other hand, in the afternoon, both shifts in cloud

739 states and changes in intensities contribute to the changes in LWP and α_c susceptibilities. Compared with LWP and
740 α_c susceptibilities, the daytime variation of CF susceptibility shows minimal sensitivity to changes in cloud state
741 frequency. This limited impact stems from the fact that the daytime fluctuation in cloud state frequency is
742 predominantly influenced by precipitating and non-precipitating thin clouds. Meanwhile, the daytime mean CF
743 susceptibilities for precipitating and non-precipitating thin clouds closely align, measuring at 0.08 and 0.09,
744 respectively (Fig.2c). This convergence diminishes the influence of alterations in the frequency of these two cloud
745 states.

746 In summary, the daytime variation of cloud susceptibility is largely driven by the variation in its intensity.
747 Since polar-orbiting satellites only observe the cloud responses to N_d perturbations across different cloud states at
748 their overpass time, they cannot fully capture the diurnal variation of cloud susceptibilities driven by the variation in
749 the intensity of cloud susceptibility. Given that all three cloud susceptibilities reach their daily minimum at around
750 13:30 LST, studies based on polar-orbiting satellite with overpass time at noon may underestimate the daily mean
751 value of cloud susceptibility.

752 4. Discussions

753 In this study, we quantify the susceptibility of warm boundary layer clouds to N_d perturbation using the
754 pixel-level SEVIRI cloud retrievals of each time step. For heavily precipitating clouds, LWP increases under pristine
755 condition (e.g., $N_d < 30 \text{ cm}^{-3}$, Fig.2a). For lightly precipitating and non-precipitating clouds, LWP decreases with
756 N_d . The N_d -LWP relationship found in this study is consistent with that in Gryspeerd et al. (2019) using global
757 mean cloud retrievals from MODIS and AMSR-E at coarser resolution of $1^\circ \times 1^\circ$ and daily timescale. This
758 consistency between different satellite measurements at different temporal and spatial scales greatly enhance our
759 confidence in the retrieved relationship.

760 This study further distinguishes non-precipitating clouds into thin and thick clouds based on their LWP. A
761 consistent decreasing trend in cloud water is found for both states, yet non-precipitating thick clouds exhibit more
762 negative LWP susceptibility ($\frac{d\ln(LWP)}{d\ln(N_d)} = -0.94$) compared to thin clouds ($\frac{d\ln(LWP)}{d\ln(N_d)} = -0.71$). The LWP
763 susceptibilities estimated in this study are more negative than those in Zhang et al. (2022) and Zhang and Feingold
764 (2023), based on similar classification of cloud states. Particularly, we found that non-precipitating thin clouds have
765 a decreasing trend in cloud water and a warming effect at the surface radiation while these are opposite in Zhang et
766 al. (2022) and Zhang and Feingold (2023). This is due to different seasons and study regions between our and their
767 studies. The summer boundary layer in the ENA region is deeper and less stable with higher cloud tops (e.g., Klein
768 and Hartmann, 1993; Ding et al., 2021; King et al., 2013) compared to the NE Pacific in Zhang et al. (2022) and the
769 NE Atlantic region in Zhang and Feingold (2023). The less stable condition, deeper boundary layer, and deeper
770 clouds could lead to a stronger cloud-top entrainment rate and result in a more negative LWP susceptibility (Possner
771 et al., 2020; Toll et al., 2019).

772 Regarding the CF adjustment to N_d perturbation, a daytime mean positive response is found for
773 precipitating and non-precipitating thin clouds and a negative response for non-precipitating thick clouds (Fig.2c).

774 Few studies have quantified the CF adjustment rate at 30-minute intervals for a direct comparison of CF
775 susceptibility. However, similar results are found using measurements and retrievals from different platforms at
776 various spatial and timescales, which greatly increase our confidence in the observed CF responses toward N_d
777 perturbation. For example, using MODIS measurement, Kaufman et al. (2005) found an increase in the longitudinal
778 mean cloudiness for warm boundary layer clouds with increasing AOD in all four regions of the Atlantic Ocean
779 characterized by distinct aerosol types. Using the natural experiment of volcanic eruption at Holuhraun in Iceland,
780 Chen et al. (2022) found that aerosols from the eruption increase the monthly mean cloud cover by 10% over the
781 North Atlantic. By tracking the cloud trajectory using geostationary satellites, Christensen et al. (2020) found that
782 aerosol enhance both CF and cloud lifetime in the timescale of 2-3 days, especially under stable conditions. It is
783 worth noting that a decrease in CF was not observed in these studies, likely due to the prevalence of non-
784 precipitating thin clouds and precipitating clouds in the Atlantic or the NE Pacific (e.g., Zhang and Feingold, 2023)
785 that mask the signal from non-precipitating thick clouds without distinguishing cloud states.

786 Lastly, the distinct “U-shaped” daytime variation in all three cloud properties found in this study (Fig.3a-c)
787 is *unlikely* due to the systematic bias in r_e and τ retrievals at large SZA based on the following two aspects. Firstly,
788 if the daytime variation is driven by retrieval bias at large SZA, we would expect the susceptibility exhibiting a
789 symmetric pattern at local noon. As shown in Figs. 10 and 6, the LWP and α_c susceptibilities for precipitating and
790 non-precipitating thick clouds exhibit asymmetric pattern at local noon: with a decreasing trend from 13 LST and a
791 daily minimum at 16 LST, and a continuously increasing trend from 11 to 18 LST, respectively. In addition, the CF
792 susceptibilities for all three cloud states show asymmetric patterns at local noon. Secondly, if the retrieval
793 uncertainty dominates the signal, we would expect less variation in cloud susceptibilities for overcast clouds, which
794 suffer less uncertainties in cloud retrievals from the plane-parallel assumption and the cloud 3-D effect. However,
795 the opposite is found from the sensitivity test where overcast clouds exhibit stronger daytime variation in cloud
796 susceptibilities (not shown).

797 5. Conclusions

798 Using N_d as an intermediary variable, this study investigates the aerosol indirect effect (AIE) for warm
799 boundary layer clouds and its daytime variation over the ENA region with the half-hourly and 3-km cloud property
800 retrievals from SEVIRI on the Meteosat-11. To constrain meteorological impacts on clouds and aerosol-cloud
801 interaction, cloud susceptibilities are estimated within a $1^\circ \times 1^\circ$ grid box for each satellite time step. Based on the
802 daytime mean cloud susceptibilities in the LWP- N_d parameter space, the sign and magnitude of cloud
803 susceptibilities strongly depend on the cloud states (Fig.2). Accordingly, warm boundary layer clouds are classified
804 into three states: precipitating clouds ($r_e > 15 \mu\text{m}$), non-precipitating thick clouds ($r_e < 15 \mu\text{m}$, $\text{LWP} > 75 \text{ gm}^{-2}$), and
805 non-precipitating thin clouds ($r_e < 15 \mu\text{m}$, $\text{LWP} < 75 \text{ gm}^{-2}$).

806 Precipitating clouds exhibit contrasting responses in cloud LWP, with increases observed for heavily
807 precipitating clouds and decreases for lightly precipitating clouds. Positive α_c and CF susceptibilities are identified
808 for both heavily and lightly precipitating clouds. The net all-sky radiative forcing of the AIE on precipitating clouds

809 is estimated to be $-13 W m^{-2} \ln(N_d)^{-1}$, with contributions from the CF and α_c effects of -9.5 and -3.5
810 $W m^{-2} \ln(N_d)^{-1}$, respectively. For non-precipitating clouds, both thick and thin clouds show negative LWP
811 susceptibility with more negative values found for thick clouds with higher LWP and N_d . This is likely attributed to
812 the stronger shortwave absorption, larger cloud top radiative cooling rate and stronger entrainment for thick clouds.
813 Consistent with the evaporation-entrainment feedback, non-precipitating thick clouds exhibit a decrease in CF and
814 α_c with increasing N_d , and results in a net warming effect at the surface and a radiative forcing of $+4.4$
815 $W m^{-2} \ln(N_d)^{-1}$. On the other hand, non-precipitating thin clouds show an increasing response in CF and a less
816 negative α_c susceptibility. Additionally, the radiative effect from increasing CF ($-8.3 W m^{-2} \ln(N_d)^{-1}$) outweighs
817 that from a darker cloud ($+3.1 W m^{-2} \ln(N_d)^{-1}$) and leads to a net cooling effect of $-5.2 W m^{-2} \ln(N_d)^{-1}$.

818 Warm boundary layer clouds manifest distinct and significant ($p < 0.05$) daytime variations in LWP, α_c , and
819 CF susceptibilities. All three cloud susceptibilities exhibit “U-shaped” diurnal patterns with clouds being less
820 susceptible in the morning and evening and more susceptible at local noon (Fig.3).

821 Daytime variation in LWP and α_c susceptibilities is likely attributed to the transition in cloud state while
822 clouds sustaining the memory of responses to N_d of the previous state (H1 in Table 1). From morning to noon, with
823 increasing solar radiation, non-precipitating thick clouds evolve to thin clouds. Thin clouds decayed from thick show
824 significantly more negative LWP and α_c susceptibilities than thin clouds that are previously thin (Fig.5). Therefore,
825 LWP and α_c susceptibilities decrease from morning to noon for thin clouds and reach their daily minima at noon
826 (Fig.4). In the afternoon, thin clouds develop to thick clouds while retaining the memory of less susceptible to N_d
827 perturbations (Fig.7) and therefore leads to an increase in LWP and α_c susceptibilities for nonprecipitating thick
828 clouds in the afternoon (Fig.6). Meanwhile, daytime variation in CF susceptibility for non-precipitating thick clouds
829 is more likely driven by changes in cloud morphology rather than the transition of cloud state (Fig.8, H3 in Table 1).
830 Compared to non-precipitating clouds, precipitating clouds exhibit smaller daytime variation in cloud susceptibility
831 (Fig.10).

832 The daytime variation in cloud susceptibility is primarily driven by changes in the intensity of cloud
833 susceptibilities from morning to noon, rather than changes in the frequency of occurrence of different cloud states
834 (Fig.12). As the polar-orbiting satellites only observe cloud susceptibilities across different cloud states during a
835 specific overpass time, they overlook the change in the intensity of cloud susceptibilities during the day. More
836 specifically, based on the daytime variation of cloud susceptibilities found in this study, LWP susceptibility
837 estimated at 13:30 LST could underestimate the daytime mean value by 26.3% (-0.76 compared to -0.60),
838 underestimate the α_c susceptibility by 475% (-0.023 compared to -0.004), and underestimate the CF susceptibility
839 by 120% (-0.019 compared to $+0.055$). It is worth noting that both the daytime variation and the daytime mean
840 values of cloud susceptibilities in this study are estimated based on the regression analysis on spatial data within
841 each satellite time step, with the assumption that the temporal change of cloud properties from N_d perturbations can
842 be represented by the spatial relationships.

843 This study underscores the importance of considering the diurnal cycle of cloud susceptibilities when
844 quantifying AIE and their impacts on clouds and radiation. The classification of cloud states enables us to
845 distinguish the sign, magnitude, and underlying processes driving the diurnal variation of AIE.

846 To further advance our understanding of the diurnal variation of AIE, several avenues for future research
847 can be pursued. Firstly, it is important to address uncertainties associated with satellite retrievals, which can
848 propagate into uncertainties in the retrieved N_d , as discussed in Grosvenor et al. (2018). Future study could utilize
849 active sensors to reduce these uncertainties, particularly during nighttime conditions. Moreover, using the retrieved
850 N_d as a proxy of aerosol concentration may introduce uncertainties related to cloud processes that can act as sources
851 or sinks of N_d , potentially buffer the relationships between N_d and cloud condensation nuclei. Future investigations
852 are needed to better understand the relationships, and how they vary with different cloud processes and throughout
853 the day. Lastly, this study encompasses all warm boundary layer clouds without considering the highly diverse
854 meteorological regimes and the associated cloud types in the ENA region. Classification of the synoptic and
855 meteorological conditions associated with different cloud states and aerosol properties would contribute to a more
856 comprehensive understanding, allowing for the disentanglement of the impacts of meteorology from AIE.

857
858

859 **Data availability:**

860 SEVIRI Meteosat-11 cloud retrieval products, produced by NASA LaRC SatCORPS group, are available from the
861 Atmospheric Radiation Measurement (ARM) Data Discovery website at <https://adc.arm.gov/discovery/>, Minnis
862 Cloud Products Using Visst Algorithm (visstgridm1minnis). The ARM ground-based radar and lidar observations
863 are available from ARM Data Discovery, KAZRARSL, (arsclkazr1kollias).

864

865 **Acknowledgment:**

866 We are grateful to the Atmospheric Radiation Measurement (ARM) user facility, a U.S. Department of Energy
867 (DOE) Office of Science user facility managed by the Biological and Environmental Research Program for
868 providing ARM observation data and archiving SEVIRI Meteosat-11 cloud retrieval products. We mainly used the
869 computing resources from the National Energy Research Scientific Computing Center (NERSC), which is supported
870 by the Office of Science of the U.S. Department of Energy under Contract No. DE-AC02-05CH11231. We
871 appreciate the constructive comments from two anonymous reviewers that helped improve the manuscript. This
872 work was performed under the auspices of the U.S. DOE by LLNL under contract DE-AC52-07NA27344. (LLNL-
873 JRNL-851496)

874

875 **Financial support:**

876 This work is supported by the DOE Office of Science Early Career Research Program and the ASR Program. DP
877 acknowledges the support of the NASA CloudSat CALIPSO Science Reconnect Program.

878

879 **Competing interests:**

880 The authors declare that they have no conflict of interest.

881

882

883 **References**

- 884 Albrecht, B. A.: Aerosols, Cloud Microphysics, and Fractional Cloudiness, *Science*, 245, 1227–1230,
885 <https://doi.org/10.1126/science.245.4923.1227>, 1989.
- 886 Arola, A., Lipponen, A., Kolmonen, P., Virtanen, T. H., Bellouin, N., Grosvenor, D. P., Gryspeerdt, E., Quaas, J., &
887 Kokkola, H. (2022). Aerosol effects on clouds are concealed by natural cloud heterogeneity and satellite
888 retrieval errors. *Nature Communications*, 13(1), 7357. <https://doi.org/10.1038/s41467-022-34948-5>
- 889 Bannartz, R.: Global assessment of marine boundary layer cloud droplet number concentration from satellite, *J. Geophys.*
890 *Res.*, 112, D02201, doi:10.1029/2006JD007547, 2007.
- 891 Bannartz, R. and Rausch, J.: Global and regional estimates of warm cloud droplet number concentration based on 13
892 years of AQUA-MODIS observations, *Atmos. Chem. Phys.*, 17, 9815–9836, [https://doi.org/10.5194/acp-17-](https://doi.org/10.5194/acp-17-9815-2017)
893 9815-2017, 2017.
- 894 Bréon, F.-M., Tanré, D., and Generoso, S.: Aerosol effect on cloud droplet size monitored from satellite, *Science*,
895 295, 834–838, 2002.
- 896 Boers, R., and R. M. Mitchell: Absorption feedback in stratocumulus clouds: Influence on cloud top albedo. *Tellus*,
897 46A, 229–241, 1994. Bretherton, C. S., Blossey, P. N., and Uchida, J.: Cloud droplet sedimentation, entrainment
898 efficiency, and subtropical stratocumulus albedo, *Geophys. Res. Lett.*, 34, L03813,
899 <https://doi.org/10.1029/2006GL027648>, 2007.
- 900 Brenguier, J. L., Burnet, F., & Geoffroy, O.: Cloud optical thickness and liquid water path – does the coefficient
901 vary with droplet concentration? *Atmospheric Chemistry and Physics*, 11(18), 9771–9786.
902 <https://doi.org/10.5194/acp-11-9771-2011>, 2011
- 903 Chen, Y.-C., Christensen, M., Stephens, G. L., and Seinfeld, J. H.: Satellite-based estimate of global aerosol–cloud
904 radiative forcing by marine warm clouds, *Nature Geosci.*, 7, 643–646, <https://doi.org/10.1038/ngeo2214>, 2014.
- 905 Chen, Y., Haywood, J., Wang, Y., Malavelle, F., Jordan, G., Partridge, D., Fieldsend, J., De Leeuw, J., Schmidt, A.,
906 Cho, N., Oreopoulos, L., Platnick, S., Grosvenor, D., Field, P., & Lohmann, U.: Machine learning reveals
907 climate forcing from aerosols is dominated by increased cloud cover. *Nature Geoscience*, 15(8), 609–614, 2022.
908 <https://doi.org/10.1038/s41561-022-00991-6>
- 909 Christensen, M. W., Jones, W. K., and Stier, P.: Aerosols enhance cloud lifetime and brightness along the stratus-
910 tocumulus transition, *P. Natl. Acad. Sci. USA*, 117, 17591–17598, <https://doi.org/10.1073/pnas.1921231117>,
911 2020.
- 912 Comstock, K. K., Wood, R., Yuter, S. E., and Bretherton, C. S.: Reflectivity and rain rate in and below drizzling
913 stratocumulus, *Q. J. Roy. Meteorol. Soc.*, 130, 2891–2918, doi:10.1256/qj.03.187, 2004.
- 914 Ding, F., Iredell, L., Theobald, M., Wei, J., & Meyer, D. : PBL Height From AIRS, GPS RO, and MERRA-2
915 Products in NASA GES DISC and Their 10-Year Seasonal Mean Intercomparison. *Earth and Space Science*,
916 8(9). <https://doi.org/10.1029/2021ea001859>, 2021
- 917 Dong, X., Xi, B., Kennedy, A., Minnis, P., & Wood, R.: A 19-month record of marine aerosol–cloud–radiation
918 properties derived from DOE ARM mobile facility deployment at the Azores. Part I: Cloud fraction and single-

919 layered MBL cloud properties. *Journal of Climate*, 27(10), 3665–3682. [https://doi.org/10.1175/JCLI-D-13-](https://doi.org/10.1175/JCLI-D-13-00553.1)
920 00553.1, 2014.

921 Dong, X., Xi, B., Qiu, S., Minnis, P., Sun-Mack, S., & Rose, F. : A radiation closure study of Arctic stratus cloud
922 microphysical properties using the collocated satellite-surface data and Fu-Liou radiative transfer model.
923 *Journal of Geophysical Research: Atmospheres*, 121(17), 10,175-110,198.
924 <https://doi.org/10.1002/2016jd025255>, 2016

925 Dong, X., Zheng, X., Xi, B., & Xie, S.: A Climatology of Midlatitude Maritime Cloud Fraction and Radiative Effect
926 Derived from the ARM ENA Ground-Based Observations. *Journal of Climate*, 36(2), 531–546,
927 <https://doi.org/10.1175/JCLI-D-22-0290.1>, 2023.

928 Duong, H. T., Sorooshian, A., and Feingold, G.: Investigating potential biases in observed and modeled metrics of
929 aerosol-cloud precipitation interactions, *Atmos. Chem. Phys.*, 11, 4027–4037, doi:10.5194/acp-11-4027-2011,
930 2011.

931 Fan, J. W., Wang, Y., Rosenfeld, D., and Liu, X. H.: Review of aerosol-cloud interactions: mechanisms,
932 significance, and challenges, *J. Atmos. Sci.*, 73, 4221–4252, 2016.

933 Feingold G, Eberhard W, Veron D, Previdi M. First measurements of the Twomey indirect effect using ground-
934 based remote sensors. *Geophys Res Lett*. 30 (6). <https://doi.org/10.1029/2002GL016633>, 2003.

935 Feingold, G., Goren, T., & Yamaguchi, T. (2022). Quantifying albedo susceptibility biases in shallow clouds.
936 *Atmospheric Chemistry and Physics*, 22(5), 3303–3319. <https://doi.org/10.5194/acp-22-3303-2022>.

937 Fons, E., Runge, J., Neubauer, D., & Lohmann, U.: Stratocumulus adjustments to aerosol perturbations disentangled
938 with a causal approach. *npj Climate and Atmospheric Science*, 6(1), 130, 2023

939 Glassmeier, F., Hoffmann, F., Johnson, J. S., Yamaguchi, T., Carslaw, K. S., and Feingold, G.: Aerosol-cloud-
940 climate cooling overestimated by ship-track data, *Science*, 371, 485–489,
941 <https://doi.org/10.1126/science.abd3980>, 2021.

942 Grosvenor, D. P., & Wood, R.: The effect of solar zenith angle on MODIS cloud optical and microphysical
943 retrievals within marine liquid water clouds. *Atmospheric Chemistry and Physics*, 14(14), 7291-7321.
944 <https://doi.org/10.5194/acp-14-7291-2014>, 2014

945 Grosvenor, D. P., Sourdeval, O., Zuidema, P., Ackerman, A., Alexandrov, M. D., Bennartz, R., Boers, R., Cairns,
946 B., Chiu, J. C., Christensen, M., Deneke, H., Diamond, M., Feingold, G., Fridlind, A., H \ddot{A} Oenerbein, A., Knist,
947 C., Kollias, P., Marshak, A., McCoy, D., Merk, D., Painemal, D., Rausch, J., Rosenfeld, D., Russchenberg, H.,
948 Seifert, P., Sinclair, K., Stier, P., van Diedenhoven, B., Wendisch, M., Werner, F., Wood, R., Zhang, Z., and
949 Quaas, J.: Remote Sensing of Droplet Number Concentration in Warm Clouds: A Review of the Current State
950 of Knowledge and Perspectives, *Rev. Geophys.*, 56, 409–453, <https://doi.org/10.1029/2017RG000593>, 2018.

951 Gryspeerdt, E., Quaas, J., and Bellouin, N.: Constraining the aerosol influence on cloud fraction, *J. Geophys. Res.-*
952 *Atmos.*, 121, 3566– 3583, <https://doi.org/10.1002/2015JD023744>, 2016.

953 Gryspeerdt, E., Goren, T., Sourdeval, O., Quaas, J., Mülmenst.dt, J., Dipu, S., Unglaub, C., Gettelman, A., and
954 Christensen, M.: Constraining the aerosol influence on cloud liquid water path, *Atmos. Chem. Phys.*, 19, 5331–
955 5347, <https://doi.org/10.5194/acp-19-5331-2019>, 2019.

956 Gryspeerd, E., Goren, T., and Smith, T. W. P.: Observing the timescales of aerosol–cloud interactions in snapshot
957 satellite images, *Atmos. Chem. Phys.*, 21, 6093–6109, <https://doi.org/10.5194/acp-21-6093-2021>, 2021.

958 Gryspeerd, E., McCoy, D. T., Crosbie, E., Moore, R. H., Nott, G. J., Painemal, D., Small-Griswold, J., Sorooshian,
959 A., and Ziemba, L.: The impact of sampling strategy on the cloud droplet number concentration estimated from
960 satellite data, *Atmos. Meas. Tech.*, 15, 3875–3892, <https://doi.org/10.5194/amt-15-3875-2022>, 2022.

961 Han, Q., Rossow, W. B., Zeng, J., and Welch, R.: Three Different Behaviors of Liquid Water Path of Water Clouds
962 in Aerosol–Cloud Interactions, *J. Atmos. Sci.*, 59, 726–735, [https://doi.org/10.1175/1520-0469\(2002\)059<0726:TDBOLW>2.0.CO;2](https://doi.org/10.1175/1520-0469(2002)059<0726:TDBOLW>2.0.CO;2), 2002.

964 Kaufman, Y. J., Koren, I., Remer, L. A., Rosenfeld, D., & Rudich, Y.: The effect of smoke, dust, and pollution
965 aerosol on shallow cloud development over the Atlantic Ocean. *Proc Natl Acad Sci U S A*, 102(32), 11207-
966 11212. <https://doi.org/10.1073/pnas.0505191102>, 2005

967 King, M. D., Platnick, S., Menzel, W. P., Ackerman, S. A., & Hubanks, P. A.: Spatial and Temporal Distribution of
968 Clouds Observed by MODIS Onboard the Terra and Aqua Satellites. *IEEE Transactions on Geoscience and*
969 *Remote Sensing*, 51(7), 3826-3852. <https://doi.org/10.1109/tgrs.2012.2227333>, 2013

970 Klein, S. A., & Hartmann, D. L.: The seasonal cycle of low stratiform clouds. *Journal of Climate*, 6(8), 1587–1606.
971 [https://doi.org/10.1175/1520-0442\(1993\)006<1587:tscols>2.0.co;2](https://doi.org/10.1175/1520-0442(1993)006<1587:tscols>2.0.co;2), 1993.

972 Liu, J., Li, Z., and Cribb, M.: Response of marine boundary layer cloud properties to aerosol perturbations
973 associated with meteorological conditions from the 19-month AMF-Azores campaign, *J. Atmos. Sci.*, 73, 4253–
974 4268, <https://doi.org/10.1175/JAS-D-15-0364.1>, 2016.

975 Mather, J. H., & Voyles, J. W.: The Arm Climate Research Facility: A Review of Structure and Capabilities, *Bull.*
976 *Am. Meteorol. Soc.*, 94, 377-392, <https://doi.org/10.1175/BAMS-D-11-00218.1>, 2013.

977 Mechem, D. B., Wittman, C. S., Miller, M. A., Yuter, S. E., and De Szoek, S. P.: Joint synoptic and cloud
978 variability over the Northeast Atlantic near the Azores, *J. Appl. Meteorol. Clim.*, 57, 1273–1290, 2018.

979 Minnis, P., Sun-Mack, S., Young, D. F., Heck, P. W., Garber, D. P., Chen, Y., Spangenberg, D. A., Arduini, R. F.,
980 Trepte, Q. Z., Smith, W. L., Ayers, J. K., Gibson, S. C., Miller, W. F., Hong, G., Chakrapani, V., Takano, Y.,
981 Liou, K., Xie, Y., and Yang, P.: CERES edition-2 cloud property retrievals using TRMM VIRS and Terra and
982 Aqua MODIS data–Part I: Algorithms, *IEEE Trans. Geosci. Remote Sens.*, 49, 4374–4400,
983 <https://doi.org/10.1109/TGRS.2011.2144601>, 2011.

984 Minnis, P., K. Bedka, Q. Trepte, C. R. Yost, S. T. Bedka, B. Scarino, K. Khlopenkov, and M. M. Khaiyer: A
985 consistent long-term cloud and clear-sky radiation property dataset from the Advanced Very High Resolution
986 Radiometer (AVHRR). Climate Algorithm Theoretical Basis Document (C-ATBD), CDRP-ATBD-0826 Rev 1
987 - NASA, NOAA CDR Program, 159 pp., DOI:10.789/V5HT2M8T,
988 https://www1.ncdc.noaa.gov/pub/data/sds/cdr/CDRs/AVHRR_Cloud_Properties_NASA/AlgorithmDescription_01B-30b.pdf, 2016.

989

990 Minnis, P., Sun-Mack, S., Chen, Y., Chang, F., Yost, C. R., Smith, W. L., Heck, P. W., Arduini, R. F., Bedka, S. T.,
991 Yi, Y., Hong, G., Jin, Z., Painemal, D., Palikonda, R., Scarino, B. R., Spangenberg, D. A., Smith, R. A., Trepte,

992 Q. Z., Yang, P., and Xie, Y.: CERES MODIS Cloud Product Retrievals for Edition 4–Part I: Algorithm
993 Changes, *IEEE T. Geosci. Remote*, 11152, 1–37, <https://doi.org/10.1117/12.2532931>, 2020.

994 Morrison, H., van Lier-Walqui, M., Fridlind, A. M., Grabowski, W. W., Harrington, J. Y., Hoose, C., et al.:
995 Confronting the challenge of modeling cloud and precipitation microphysics. *Journal of Advances in Modeling*
996 *Earth Systems*, 12, e2019MS001689. <https://doi.org/10.1029/2019MS001689>, 2020.

997 Painemal, D., Minnis, P., and Sun-Mack, S.: The impact of horizontal heterogeneities, cloud fraction, and liquid
998 water path on warm cloud effective radii from CERES-like Aqua MODIS retrievals, *Atmos. Chem. Phys.*, 13,
999 9997–10003, <https://doi.org/10.5194/acp-13-9997-2013>, 2013.

1000 Painemal, D.: Global Estimates of Changes in Shortwave Low-Cloud Albedo and Fluxes Due to Variations in Cloud
1001 Droplet Number Concentration Derived From CERES-MODIS Satellite Sensors, *Geophys. Res. Lett.*, 45,
1002 9288–9296, <https://doi.org/10.1029/2018GL078880>, 2018.

1003 Painemal, D., Spangenberg, D., Smith Jr., W. L., Minnis, P., Cairns, B., Moore, R. H., Crosbie, E., Robinson, C.,
1004 Thornhill, K. L., Winstead, E. L., and Ziemba, L.: Evaluation of satellite retrievals of liquid clouds from the
1005 GOES-13 imager and MODIS over the midlatitude North Atlantic during the NAAMES campaign, *Atmos.*
1006 *Meas. Tech.*, 14, 6633–6646, <https://doi.org/10.5194/amt-14-6633-2021>, 2021.

1007 Penner, J. E., Dong, X., and Chen, Y.: Observational evidence of a change in radiative forcing due to the indirect
1008 aerosol effect, *Nature*, 427, 231–234, 2004.

1009 Petters, J. L., J. Y. Harrington, and E. E. Clothiaux: Radiative–Dynamical Feedbacks in Low Liquid Water Path
1010 Stratiform Clouds. *J. Atmos. Sci.*, 69, 1498–1512, <https://doi.org/10.1175/JAS-D-11-0169.1>, 2012.

1011 Possner, A., Eastman, R., Bender, F., & Glassmeier, F.: Deconvolution of boundary layer depth and aerosol
1012 constraints on cloud water path in subtropical stratocumulus decks. *Atmospheric Chemistry and Physics*, 20(6),
1013 3609-3621. <https://doi.org/10.5194/acp-20-3609-2020>, 2020

1014 Rémillard, J., Kollias, P., Luke, E., and Wood, R.: Marine Boundary Layer Cloud Observations in the Azores, *J.*
1015 *Climate*, 25, 7381–7398, <https://doi.org/10.1175/JCLI-D-11-00610.1>, 2012.

1016 Sandu, I., Brenguier, J., Geoffroy, O., Thouron, O., and Masson, V.: Aerosol impacts on the diurnal cycle of marine
1017 stratocumulus, *J. Atmos. Sci.*, 65, 2705–2718, 2008.

1018 Sandu, I., Brenguier, J.-L., Thouron, O., and Stevens, B.: How important is the vertical structure for the
1019 representation of aerosol impacts on the diurnal cycle of marine stratocumulus? *Atmos. Chem. Phys.*, 9, 4039–
1020 4052, doi:10.5194/acp-9-4039-2009, 2009.

1021 Sato, Y., Goto, D., Michibata, T., Suzuki, K., Takemura, T., Tomita, H., and Nakajima, T.: Aerosol effects on cloud
1022 water amounts were successfully simulated by a global cloud-system resolving model, *Nat. Commun.*, 9, 985,
1023 <https://doi.org/10.1038/s41467-018-03379-6>, 2018.

1024 Small, J., Chuang, P., Feingold, G. & Jiang, H.: Can aerosol decrease cloud lifetime? *Geophys. Res. Lett.* 36,
1025 L16806, 2009.

1026 Stevens, B. and Feingold, G.: Untangling aerosol effects on clouds and precipitation in a buffered system, *Nature*,
1027 461, 607–613, doi:10.1038/nature08281, 2009.

1028 Stevens, B. & Seifert, A.: Understanding the macrophysical outcomes of microphysical choices in simulations of
 1029 shallow cumulus convection. *J. Meteorol. Soc. Jpn* 86A, 141–163, 2008.

1030 Sun-Mack, S., Minnis, P., Chen, Y., Kato, S., Yi, Y., Gibson, S. C., et al.: Regional apparent boundary layer lapse
 1031 rates determined from CALIPSO and MODIS data for cloud-height determination. *Journal of Applied*
 1032 *Meteorology and Climatology*, 53(4), 990–1011, 2014.

1033 Terai, C. R., Wood, R., Leon, D. C., and Zuidema, P.: Does precipitation susceptibility vary with increasing cloud
 1034 thickness in marine stratocumulus? *Atmos. Chem. Phys.*, 12, 4567–4583, doi:10.5194/acp-12-4567-2012, 2012.

1035 Terai, C. R., Wood, R., and Kubar, T. L.: Satellite estimates of precipitation susceptibility in low-level marine
 1036 stratiform clouds, *J. Geophys. Res.*, 120, 8878–8889, doi:10.1002/2015JD023319, 2015.

1037 Toll, V., Christensen, M., Quaas, J., and Bellouin, N.: Weak average liquid-cloud-water response to anthropogenic
 1038 aerosols, *Nature*, 572, 51–55, <https://doi.org/10.1038/s41586-019-1423-9>, 2019.

1039 Trepte, Q. Z., and Coauthors: Global cloud detection for CERES edition 4 using Terra and Aqua MODIS data. *IEEE*
 1040 *Trans. Geosci. Remote Sens.*, 57, 9410–9449, <https://doi.org/10.1109/TGRS.2019.2926620>, 2019.

1041 Twomey, S.: The Influence of Pollution on the Shortwave Albedo of Clouds, *J. Atmos. Sci.*, 34, 1149–1152,
 1042 [https://doi.org/10.1175/1520-0469\(1977\)034<1149:TIOPOP>2.0.CO;2](https://doi.org/10.1175/1520-0469(1977)034<1149:TIOPOP>2.0.CO;2), 1977.

1043 Wang, S., Wang, Q., and Feingold, G.: Turbulence, Condensation, and Liquid Water Transport in Numerically
 1044 Simulated Nonprecipitating Stratocumulus Clouds, *J. Atmos. Sci.*, 60, 262–278, [https://doi.org/10.1175/1520-0469\(2003\)060<0262:TCALWT>2.0.CO;2](https://doi.org/10.1175/1520-0469(2003)060<0262:TCALWT>2.0.CO;2), 2003.

1046 Wang, Y., Zheng, X., Dong, X., Xi, B., Wu, P., Logan, T., and Yung, Y. L.: Impacts of long-range transport of
 1047 aerosols on marine boundary-layer clouds in the eastern North Atlantic, *Atmos. Chem. Phys.*, 20, 14741–14755,
 1048 <https://doi.org/10.5194/acp-20-14741-2020>, 2020.

1049 Warren, S. G., C. J. Hahn, J. London, R. M. Chervine, and R. L. Jenne: Global distribution of total cloud cover and
 1050 cloud type amounts over ocean, Tech. Note NCAR/TN-317 + STR, 42, Natl. Cent. for Atmos. Res., Boulder,
 1051 Colo., <https://doi.org/10.2172/5415329>, 1988.

1052 Williams, A. S., & Igel, A. L.: Cloud top radiative cooling rate drives non-precipitating stratiform cloud responses to
 1053 aerosol concentration. *Geophysical Research Letters*, 48, e2021GL094740.
 1054 <https://doi.org/10.1029/2021GL094740>, 2021.

1055 Wood, R.: Stratocumulus Clouds, *Mon. Weather Rev.*, 140, 2373–2423, <https://doi.org/10.1175/MWR-D-11-00121.1>, 2012.

1057 Wu, P., Dong, X., Xi, B., Tian, J., & Ward, D. M.: Profiles of MBL cloud and drizzle microphysical properties
 1058 retrieved from ground-based observations and validated by aircraft in situ measurements over the Azores.
 1059 *Journal of Geophysical Research: Atmospheres*, 125, e2019JD032205. <https://doi.org/10.1029/2019JD032205>,
 1060 2020.

1061 Wu, P., X. Dong, and B. Xi: A climatology of marine boundary layer cloud and drizzle properties derived from
 1062 ground-based observations over the Azores. *J. Climate*, 33, 10133–10148, <https://doi.org/10.1175/JCLI-D-20-0272.1>, 2020.

1064 Xi, B., Dong, X., Minnis, P., & Khaiyer, M. M.: A 10 year climatology of cloud fraction and vertical distribution
1065 derived from both surface and GOES observations over the DOE ARM SPG site. *Journal of Geophysical*
1066 *Research*, 115(D12). <https://doi.org/10.1029/2009jd012800>, 2010

1067 Xue, H. and Feingold, G.: Large-Eddy Simulations of Trade Wind Cumuli: Investigation of Aerosol Indirect Effects,
1068 *J. Atmos. Sci.*, 63, 1605–1622, <https://doi.org/10.1175/JAS3706.1>, 2006.

1069 Yeom, J. M., Yum, S. S., Shaw, R. A., La, I., Wang, J., Lu, C., et al.: Vertical variations of cloud microphysical
1070 relationships in marine stratocumulus clouds observed during the ACE ENA campaign. *Journal of Geophysical*
1071 *Research: Atmospheres*, 126, e2021JD034700. <https://doi.org/10.1029/2021JD034700>, 2021.

1072 Zhang, Z., Song, Q., Mechem, D. B., Larson, V. E., Wang, J., Liu, Y., Witte, M. K., Dong, X., and Wu, P.: Vertical
1073 dependence of horizontal variation of cloud microphysics: observations from the ACE-ENA field campaign and
1074 implications for warm-rain simulation in climate models, *Atmos. Chem. Phys.*, 21, 3103–3121,
1075 <https://doi.org/10.5194/acp-21-3103-2021>, 2021.

1076 Zhang, J., Zhou, X., Goren, T., and Feingold, G.: Albedo susceptibility of northeastern Pacific stratocumulus: the
1077 role of covarying meteorological conditions, *Atmos. Chem. Phys.*, 22, 861–880, [https://doi.org/10.5194/acp-22-](https://doi.org/10.5194/acp-22-861-2022)
1078 [861-2022](https://doi.org/10.5194/acp-22-861-2022), 2022.

1079 Zhang, J., and Feingold, G.: Distinct regional meteorological influences on low-cloud albedo susceptibility over
1080 global marine stratocumulus regions, *Atmos. Chem. Phys.*, 23, 1073–1090, [https://doi.org/10.5194/acp-23-](https://doi.org/10.5194/acp-23-1073-2023)
1081 [1073-2023](https://doi.org/10.5194/acp-23-1073-2023), 2023.

1082 Zheng, Q., and Miller, M. A.: Summertime Marine Boundary Layer Cloud, Thermodynamic, and Drizzle
1083 Morphology over the Eastern North Atlantic: A Four-Year Study, *J. Climate*, 35, 4805-4825,
1084 <https://doi.org/10.1175/JCLI-D-21-0568.1>, 2022.

1085 Zheng, X. J., B. K. Xi, X. Q. Dong, P. Wu, T. Logan, and Y. Wang, 2022: Environmental effects on aerosol–cloud
1086 interaction in non-precipitating marine boundary layer (MBL) clouds over the eastern North Atlantic.
1087 *Atmospheric Chemistry and Physics*, 22, 335–354, <https://doi.org/10.5194/acp-22-335-2022>.

1088 Zhou, X., Zhang, J., & Feingold, G.: On the importance of sea surface temperature for aerosol-induced brightening
1089 of marine clouds and implications for cloud feedback in a future warmer climate. *Geophysical Research Letters*,
1090 48, e2021GL095896. <https://doi.org/10.1029/2021GL095896>, 2021.

1091 Zhou, X., & Feingold, G. (2023). Impacts of mesoscale cloud organization on aerosol-induced cloud water
1092 adjustment and cloud brightness. *Geophysical Research Letters*, 50, e2023GL103417.
1093 <https://doi.org/10.1029/2023GL103417>

1094 Zuidema, P., Leon, D., Pazmany, A., & Cadeddu, M.: Aircraft millimeter-wave passive sensing of cloud liquid
1095 water and water vapor during VOCALS-REx. *Atmospheric Chemistry and Physics*, 12(1), 355-369.
1096 <https://doi.org/10.5194/acp-12-355-2012>, 2012

1097

1098